Optimal Estimation Retrieval Framework for Daytime Clear-Sky Total Column Water Vapour from MTG-FCI Near-Infrared Measurements

Jan El Kassar[1,3], Cintia Carbajal Henken[1], Xavier Calbet[2], Pilar Rípodas[2], Rene Preusker[1], and Jürgen Fischer[1,3]

[1]Institute of Meteorology, Freie Universität Berlin, Carl-Heinrich-Becker-Weg 6-10, 12165 Berlin, Germany
[2]Agencia Estatal de Meteorología, Leonardo Prieto Castro 8, Ciudad Universitaria, 28071 Madrid, Spain
[3]Spectral Earth GmbH, Baseler Str. 91a, 12205 Berlin, Germany

Correspondence: Jan El Kassar, jan.elkassar@met.fu-berlin.de; Tel.: +49-30-838-64876

Abstract. A retrieval of total column water vapour (TCWV) from the new daytime, clear-sky near-infrared measurements of the Flexible Combined Imager (FCI) on-board the geostationary satellite Meteosat Third Generation Imager (MTG-I, Meteosat-12) is presented. The retrieval algorithm is based on the differential absorption technique, relating TCWV amounts to the radiance ratio of a non-absorbing band at 0.865 ~~μm~~ µm and a nearby ~~water vapour (WV)~~ WV absorbing band at 0.914 ~~μm~~µm. The sensitivity of the band ratio to WV amount increases towards the surface, which means the whole atmospheric column down to the boundary layer moisture variability can be observed well.

The retrieval framework is based on an Optimal Estimation (OE) method providing pixel-based uncertainty estimates. It builds on well-established algorithms successfully applied to other passive imagers with similar spectral band settings. Transferring knowledge gained in their development onto FCI required some new approaches. The absence of additional, adjacent window bands to estimate the surface reflectance within FCI's absorbing channel ~~were~~ are mitigated using a ~~Principle~~ Principal Component Regression (PCR) from the bands at 0.51, 0.64, 0.865, 1.61, and 2.25 ~~μm~~µm.

~~Since a~~ We utilize synergistic observations from OLCI and SLSTR to generate "FCI-like" measurements. OLCI bands were complemented with SLSTR observations, enabling evaluation of the retrieval's robustness and global performance of the PCR. Furthermore, this enables algorithm testing under realistic conditions using well-characterized data, at a time when a long-term~~calibrated FCI dataset is not available yet , we build a second~~ , fully calibrated FCI Level 1c dataset was not yet available. We build a forward model for two FCI equivalent NIR bands (0.865 and 0.9 ~~μm~~µm) on the Sentinel-3 Ocean and Land Colour Instrument (OLCI). A long-term validation of OLCI against a single Atmospheric Radiation Measurement (ARM) reference site without the PCR resulted in a bias of 1.85 kg/m^2, cRMSD of 1.26 kg/m^2 and R^2 of 0.995. ~~In order to test the PCR which uses FCI bands in the visible to short-wave infrared, we replaced the bands missing in OLCI with bands from the Sea and Land Surface Temperature Radiometer (SLSTR). A spectrally similar dataset was created from SLSTR and OLCI data on Sentinel-3A/B during June 2021. This dataset is used to test the retrieval with regards to robustness and global performance of the PCR. A~~

A first verification of ~~this~~ the OLCI/SLSTR "~~FCI-alike~~FCI-like" TCWV against well-established ground-based TCWV products concludes with a wet bias between ~~1.23~~ 0.33 – ~~3.12~~ 2.84 kg/m^2, a cRMSD between ~~1.88~~ 1.46 – ~~2.35~~ 2.21 kg/m^2 and R^2 between ~~0.95~~ 0.98 – ~~0.97~~0.99. In this set of ~~comparison~~comparisons, only land pixels were considered. Furthermore, a dataset of FCI Level 1c observations with a preliminary calibration was processed. The TCWV processed ~~from FCI data~~ for these FCI measurements aligns well with reanalysis TCWV and collocated OLCI/SLSTR TCWV but show a dry bias. A more rigorous validation and assessment will be done ~~,~~once a longer record of FCI data is available.

~~The PCR may be extended to include more diverse water-bodies. In future iterations, more bands in the visible spectral range may be added to further increase performance in presence of aerosol over dark surfaces.~~

~~This novel TCWV dataset~~ TCWV observations derived from geostationary satellite ~~observations enhances~~ measurements enhance monitoring of WV distributions and associated meteorological phenomena from synoptic scales down to local scales. Such observations are of special interest for the advancement of nowcasting techniques and Numerical Weather Prediction (NWP) accuracy as well as process-studies.

1 Introduction

~~The new Meteosat Third Generation Imager (MTG-I, hereinafter referred to as MTG) carries the Flexible Combined Imager (FCI) (Holmlund et al., 2021; Martin et al., 2021). This third generation of European geostationary meteorological satellites is commissioned by the European Organisation for the Exploitation of Meteorological Satellites (EUMETSAT) for monitoring weather and climate. FCI is the successor to the Spinning Enhanced Visible and Infrared Imager (SEVIRI) (Schmetz et al., 2002) and will both enhance the temporal and spatial resolution of geostationary remote sensing observations. Also, an expanded set of spectral channels compared to SEVIRI allows for more comprehensive observations of atmospheric and surface properties. Even more compelling is, that the instrument FCI which measures radiances across the visible (VIS), near-~~

Water vapour (WV) is the fundamental ingredient in the formation of clouds and precipitation. Spatio-temporal WV distributions and fluxes impact the intensity and duration of precipitation. The presence of sufficient low-level moisture in the atmospheric boundary layer facilitates the formation of convective development through enhancement of atmospheric instability and also contributes to storm severity by acting as a source of energy, once a storm has initiated (e.g., Johns and Doswell, 1992; Doswell et al., 1996; . On a global, climatological scale, WV is a major contributor to global energy fluxes and, ~~shortwave-, midwave- and~~longwave-infrared ~~spectra, includes a new band not available on any other instrument onboard a geostationary platform to date. This band is located within one of the $\rho\sigma\tau$ water vapour (WV) absorption regions in the Near-Infrared (NIR) at 0.913 μm. There, light is more likely to be absorbed by WV molecules compared to spectral regions outside these absorption features (window regions)~~due to its abundance and absorption over a wide range of the solar and terrestrial spectrum, acts as the strongest greenhouse gas (e.g. Trenberth et al., 2003; Schmidt et al., 2010). Within a changing climate, a warmer atmosphere will contain more WV which may form a positive feedback loop and further enhance global warming. Moreover, ~~these NIR measurements exhibit the greatest sensitivity to WV amounts near the surface. Consequently, this allows for probing the entire atmospheric column, thus the retrieval of accurate clear-sky~~ a moister atmosphere is predicted to produce more severe weather (e.g., Allen and Ingram, 2

. Apart from that, WV is considered an inconvenient atmospheric component for several remote sensing applications for which precise information on WV amounts in the atmosphere are needed for atmospheric correction methods (e.g. Gao et al., 2009; Wiegner and G

.

Observations of total column water vapour (TCWV) fields as well as providing information on changes of WV amounts in the lower troposphere. This contrasts with WV retrievals from thermal infrared measurements from satellite-based passive imagers operating in the visible (VIS), near-infrared (NIR) and thermal infrared (TIR) spectral range play a key role in monitoring its distribution at regional to global scales. WV retrievals using TIR measurements have a long heritage and are widely used, particularly from geostationary satellite platforms. On the one hand, a split-window technique using weakly absorbing WV measurements can be employed to retrieve TCWV or boundary layer WV with relatively high uncertainties (e.g., Kleespies and McMillin, 1990; Casadio et al., 2016; Hu et al., 2019; Dostalek et al., 2021; El Kassar et al., 2021). Lindsey et al. (2014) and Lindsey et al. (2018) showed that the split-window difference by itself may already provide valuable insight on the WV content in the boundary layer or lowest layers of the troposphere. On the other hand, measurements from strongly absorbing WV bands serve to retrieve WV amounts limited to upper tropospheric levels and/or layered WV products (e.g., Koenig and De Coning, 2009; Martinez et al., 2022). However, due to the absorption and re-emission of radiation by WV in the IR, such approaches rely on knowledge of the atmospheric temperature profile in addition to the atmospheric WV profile. Using observations in the VIS/NIR largely avoids these temperature-related complications.

The introduction of MTG and its new FCI NIR band, particularly in combination with increased temporal coverage of 10 minutes, greatly expands our ability to quantify and characterize local to global scale water vapour distributions and monitor their changes. This has important implications for both weather and climate research and applications. Atmospheric WV is the fundamental ingredient in the formation of clouds and precipitation. Spatio-temporal WV distributions and fluxes impact intensity and duration of precipitation processes. The presence of sufficient low-level moisture in the atmospheric boundary layer facilitates the formation of convective development through enhancement of atmospheric instability and also contributes to storm severity by acting as a source of energy, once a storm has been initiated (e.g., Johns and Doswell, 1992; Doswell et al., 1996; Fabry

.

Particularly in the domain of nowcasting, the newFCI observations , which will provide detailed and quasi real-time monitoring of boundary layer WV or TCWV and related (convective) cloud formation, could substantially advance the field (e.g., Benevides et al., 2015; Van Baelen et al., 2011; Dostalek et al., 2021). On a global, climatological scale, WV is a major contributor to global energy fluxes through the atmosphere and, due to its abundance and absorption of light over a wide range of the solar and terrestrial spectrum, acts as the strongest greenhouse gas(e.g. Trenberth et al., 2003; Schmidt et al., 2010). In the context of climate change, a warmer atmosphere will provide more use of the so-called $\rho\sigma\tau$ WV absorption region in the NIR (0.9 to 1.0 µm) is not new. This designation stems from first observations of atmospheric absorption of solar radiation in the 19th century (Langley, 1902). There, light is more likely to be absorbed by WV molecules compared to spectral regions outside these absorption features (window regions). These NIR measurements exhibit the greatest sensitivity to WV amounts near the surface. Consequently, this allows for the retrieval of accurate clear-sky TCWV fields as well as providing information on changes of WV , forming a positive feedback loop, thus further enhancing global warming. Moreover, a moister atmosphere is

predicted to produce more severe weather (e.g., Allen and Ingram, 2002; Neelin et al., 2022; Chen and Dai, 2023). Apart from that, WV is considered a inconvenient atmospheric component for several remote sensing applications, e.g., surfaceparameter retrievals, for which precise information on WV amounts in the atmosphere is needed for atmospheric correction methods (e.g. Gao et al., 2009; Wiegner and Gasteiger, 2015; Valdés et al., 2021).

The use of these NIR WV absorption measurements for TCWV retrievals is not new. lower troposphere. For several decades, the $\rho\sigma\tau$ water vapour absorption region has been researched using radiative transfer models and exploited in TCWV retrieval schemes (e.g., Fischer, 1988; Gao and J., 1992; Bennartz and Fischer, 2001; Albert et al., 2005; Lindstrot et al., 2012; Diedrich et al., 2015; Preusker et al., 2021). The focus first lay on ground-based radiometers and soon shifted to airborne and space-borne imagers. The first satellites which that carried instruments with dedicated NIR water vapour (WV) WV bands were almost exclusively on satellite platforms with sun-synchronous, polar orbits and could deliver global daily coverage at a km to hm resolution on a daily basis. Even at a km resolution, NIR TCWV is able to can resolve convective phenomena such as horizontal convective rolls or gravity waves (Carbajal Henken et al., 2015; Lyapustin et al., 2014). The Current NIR TCWV products, only available on polar orbits, provide accurate, highly-resolved TCWV but lack temporal resolution and may introduce observation biases in climatologies (Diedrich et al., 2016; Carbajal Henken et al., 2020).

The new Meteosat Third Generation Imager (MTG-I, hereinafter referred to as MTG) carries the Flexible Combined Imager (FCI) (Holmlund et al., 2021; Martin et al., 2021). The European Organisation for the Exploitation of Meteorological Satellites (EUMETSAT) commissions this third generation of European geostationary meteorological satellites for monitoring weather and climate. FCI is the successor to the Spinning Enhanced Visible and Infrared Imager (SEVIRI) (Schmetz et al., 2002) and will enhance the temporal and spatial resolution of geostationary remote sensing observations. Also, an expanded set of spectral channels compared to SEVIRI allows for more comprehensive observations of atmospheric and surface properties. FCI includes a new NIR WV absorption band not available on any other instrument onboard a geostationary platform to date. This band is located within the $\rho\sigma\tau$ WV absorption region at 0.914 µm.

The introduction of MTG and its new FCI NIR band will expand our ability to quantify and characterize local to global-scale WV distributions and monitor their changes. This has important implications for both weather and climate research and applications. Particularly in the domain of nowcasting, FCI's fine-scale observation of TCWV could substantially advance the field (e.g., Benevides et al., 2015; Van Baelen et al., 2011; Dostalek et al., 2021). The Satellite Application Facility in on Support to Nowcasting and Very Short Range Forecasting (NWCSAF) is an organisation funded by EUMETSAT and aims to support meteorological services with satellite data critical for the prediction of high-impact weather (e.g., storms, fog). They commission, develop and maintain software which utilises many weather satellite instruments, including MTG-FCI/Meteosat-12 (García-Pereda et al., 2019).

A NIR TCWV product in the portfolio of NWCSAF's software will greatly benefit the nowcsating nowcasting and meteorological community at large. Current NIR TCWV products, only available on polar orbits, provide accurate highly-resolved TCWV but lack temporal resolution and may introduce observation biases in climatologies (Diedrich et al., 2016; Carbajal Henken et al., 20 . In contrast, networks which use Global Navigation Satellite Systems (GNSS) to retrieve TCWV have good temporal coverage but lack areal context and cannot provide the coverage of a passive imager.

In this work, we present our TCWV retrieval framework utilizing the novel NIR measurements obtained from MTG-FCI. Our approach builds on established TCWV retrieval frameworks successfully applied to other passive imagers sharing similar spectral band configurations. The differential absorption technique, using the ratio of measurements in the $\rho\sigma\tau$-absorption band and ~~a nearby window band~~nearby window bands, was previously employed ~~to~~ in measurements of the Medium Resolution Imaging Spectrometer (MERIS) onboard Envisat (Bennartz and Fischer, 2001; Lindstrot et al., 2012).

~~To fill the temporal gap between observations from MERIS and its follow-up instrument Ocean and Land Colour Instrument (OLCI) on-board the Sentinel-3 satellites consistently, the optimal estimation (OE) procedure for MERIS TCWV retrievals was adapted for NIR measurements of the Moderate Resolution Imaging Spectroradiometer (MODIS) on-board Aqua and Terra satellites (Diedrich et al., 2015). More recently, with the~~ With the launch of the Copernicus Sentinel-3A and Sentinel-3B satellites (Donlon et al., 2012) and onboard ~~OLCI instruments~~Ocean and Land Colour Imager (OLCI), the retrieval framework has been extended to fully exploit OLCI's extended spectral capabilities by using multiple bands sensitive to WV absorption (Preusker et al., 2021). Operational and calibrated FCI Level 1c data only became available at the end of 2024. Due to the unique technical characteristics of ~~MTG-FCI and the absence of a lengthy and~~ FCI as well as the limited availability of a well-calibrated FCI data record at the time ~~of completion of this work~~ this work was conducted, new strategies are imperative for our methodology and its assessment. ~~Among those are an~~ One key element is the surface reflectance approximation method for the absorption band~~and~~ , which can be assessed with the use of OLCI-SLSTR ~~data to mimic FCI data for assessment. In order to test our algorithm with OLCI, the same set of simulations we do for FCI are done for~~ "FCI-like" data. In particular, we applied the same forward model and inversion principles to OLCI band 17 (0.865 ~~μm~~µm) and band 19 (0.9 ~~μm) . The same inversion technique is used for both FCIand OLCI~~µm) as were used for FCI. The use of the OLCI/SLSTR synergy provides us with a formidable opportunity to establish an adapted retrieval framework and enables a robust testbed to explore algorithm performance accordingly. Additionally, OLCI Level 1b has well-known radiometric characterization and worldwide coverage, allowing for a practical and reliable basis to assess and refine the retrieval framework under a wide range of realistic atmospheric and surface conditions.

The structure of this paper is as follows. Section 2 introduces the MTG-FCI data, OLCI-SLSTR data, auxiliary data, and the TCWV reference datasets, along with the associated matchup method. Section 3 details the MTG-FCI TCWV retrieval framework, covering the physical background, forward model, inversion method, ~~and~~ albedo approximation method integral to the algorithm, and the finalized retrieval framework. Section 4 presents the results of the matchup assessments conducted on both local and global scales, along with initial analyses using a preliminary calibrated MTG-FCI dataset and a representative case study. Section 5 provides a discussion and outlook, and Sect. 6 concludes the paper.

2 Data

2.1 MTG-FCI Data

~~Meteosat Third Generation~~ MTG is an operational EUMETSAT satellite mission ~~. It~~ which currently consists of one satellite ~~which is in a~~ in geosynchronous orbit at ~~a longitude of~~ 0° longitude. It carries the ~~Flexible Combined Imager (FCI) and the~~

Lightning Imager (LI) ~~. FCI~~ and the FCI which is a multispectral instrument ~~which~~ that scans with a fast east-west and a slow north-south motion. It has 16 bands which range from the VIS (0.44 ~~μm~~µm) to the ~~thermal infrared (TIR)~~ TIR (13.3 ~~μm~~µm). The full-disk scan service covers ~~a circular area of~~ approximately one-fourth of the Earth's surface within 10 minutes, covering Europe, Africa, and parts of the Atlantic and Indian ~~ocean~~ oceans (Durand et al., 2015; Holmlund et al., 2021). In the future, a second MTG-FCI will provide a rapid scan service, which ~~provides coverage of the upper~~ covers the northern third of the full-disk within 2.5 minutes, ~~only~~ covering parts of Europe and the Mediterranean. The spatial resolution at sub-satellite point (SSP) of one VIS band at 0.64 ~~μm~~ µm and one SWIR band at 2.25 ~~μm~~ µm is 0.5 km. The spatial resolution of the other VIS to SWIR bands and the TIR bands at 3.8 ~~μm~~ µm and 10.5 ~~μm~~ µm is 1.0 km at SSP. The remaining TIR bands have ~~a~~ an SSP resolution of 2.0 km. Due to the curvature of the Earth~~and the coverage of FCI, the real spatial resolution at ground level~~ , the actual spatial resolution outside the SSP is slightly lower. ~~For example~~E.g., the 1 km SSP resolution (VIS, NIR and 10.5 ~~μm~~µm) in Northern Europe is closer to 2.0 to 3.0 km.

MTG1 was launched successfully into orbit on 13th of December 2022, and currently the mission is still in the commissioning phase. Because of that, we use the latest release of preliminary MTG-FCI ~~level~~ Level 1c data provided by EUMETSAT in February 2024 (EUMETSAT, 2024b). They consist of one full-disk scene ~~on~~ from 13th January 2024 ~~measured~~ between 11:50 and 12:00 ~~UTCZ~~UTC. They were downloaded from EUMETSAT's sftp server at https://user.eumetsat.int/news-events/news/new-mtg-fci-test-dataset-mtgtd-505 and more ~~detail~~ details on this dataset can be found in EUMETSAT (2024a). At the time of publication, no cloud mask is readily available for the FCI test data. Therefore, we ~~build~~ built a simple cloud mask algorithm. The ~~majority of the cloud mask algorithm is~~ cloud masking algorithm is largely based on the work presented in Hünerbein et al. (2023). In this publication,n the authors adapted and extended cloud masking and typing algorithms developed for NASA's Aqua/Terra Moderate Imaging Spectrometer (MODIS) (Ackerman et al., 2002) to ESA's Cloud Aerosol and Radiation Explorer Mission (EarthCARE) Multi Spectral Imager (MSI). We adapted a subset of their tests to the FCI bands and estimated new coefficients and thresholds. Eventually, the cloud mask consists of two tests: ~~a reflectance test and a reflectance ratio or~~ threshold tests for reflectances, a reflectance ratio or the Global Environmental Monitoring Index (GEMI) ~~test Pinty and Verstraete (1992). For the reflectances, ratios and test the bands VIS_06 (0.640 μm), VIS_08 and NIR_13 were used.~~ Pinty and Verstraete (1992).

2.2 S3-OLCI/SLSTR Data

Sentinel-3 is an operational COPERNICUS satellite mission of the European Commission, managed by EUMETSAT. It consists of two sister satellites (Sentinel-3A: S3A; Sentinel-3B: S3B) which orbit the Earth at an altitude of 814.5 km, an inclination of 98.65 ° and a local equator crossing time of 10:00 AM. S3B is phase-shifted to S3A by 140 °. This way, the imaging instruments onboard the two satellites achieve global coverage almost daily. The payloads consist of the ~~SAR~~ Synthetic Aperture Radar Altimeter (SRAL), supported by the Microwave Radiometer (MWR), ~~an visible/near-infrared imager Ocean and Land Colour Instrument (OLCI) and an visible to thermal infrared imager~~ the Sea and Land Surface Temperature Radiometer (SLSTR), and OLCI.

OLCI is a push-broom multispectral imaging spectrometer ~~which~~ that consists of five cameras. It measures at 21 ~~discrete bands ranging for the~~ bands ranging from the VIS (0.4 ~~μm~~µm) to the NIR (1.02 ~~μm~~µm). The swath-width of OLCI is 1215 km at a full SSP resolution of 0.3 km per pixel, which is referred to as "Full Resolution". In the "Reduced Resolution", 4 by 4 ~~pixel~~ pixels are aggregated into ~~.~~ 1.2 km pixels. This is the resolution used in this study.

~~One OLCI instrument achieves global coverage in three days. In its current two satellite configuration almost complete global coverage is achieved within one day, with small gaps at the equator.~~ A characteristic of OLCI is an across-track spectral shift due to the five discrete cameras. This can be corrected for by taking into account the actual central wavelength at each of the across-track pixels (Preusker et al., in prep.).

SLSTR is a conical scanning multispectral, ~~multiangle~~ multi-angle radiometer. It measures at eight discrete bands ranging ~~for~~ from the mid VIS (0.55 ~~μm~~µm) to the TIR (12.02 ~~μm~~µm). The nadir-viewing swath width is 1400 km, and the oblique/rear-viewing swath width is 740 km. In the VIS ~~and SWIR bands(until 2.25 μm)~~ to SWIR bands, SLSTR has a spatial resolution of 0.5 km at SSP, in the TIR (3 ~~μm~~ µm to 12.02 ~~μm)~~µm), the spatial resolution is 1 km at SSP. ~~Similar to OLCI, SLSTR provides global coverage within two to three days in nadir view. In oblique view this is the case within three to four days. In the current two satellite~~ In the current two-satellite constellation, nadir-view global coverage is achieved within one day.

In order to mimic the capabilities of FCI at a similar spatial resolution and with similar spectral characteristics, we ~~merged some~~ collocated SLSTR observations to the OLCI grid using nearest-neighbour sampling. The ~~SLSTR bands used were bands~~ used SLSTR bands are S5 (1.612 ~~μm~~µm, 0.5 km) and S6 (2.25 ~~μm~~µm, 0.5 km). They have been mapped to OLCI's reduced resolution at 1.2 km. ~~This way, we can test how our algorithm performs globally on real data, before MTG-FCI data at nominal calibration become available publicly. The cloud-mask used to filter out cloudy pixels is the IdePIX cloudmask~~ Using Sentinel-3A and B, a representative set of swaths was created for every month of the year 2021 which amounts to a total of 1800 swaths across 80 days. The Identification of Pixel features (IdePIX) cloud detection algorithm was used to create cloud masks (Iannone et al., 2017; Wevers et al., 2021; Skakun et al., 2022).

2.3 ECMWF ERA5 Forecast and Reanalysis Data

Our TCWV retrieval is based on an inversion technique (Sec. 3) which uses a first guess, as well as a priori and ancillary parameter data. These ~~data~~ may come from a climatology or could be set to a global climatological value. However, retrieval performance can be greatly increased and ~~speeded up if data fields are passed to the algorithm which are already somewhat close~~ sped up if the a priori data are already slightly closer to the solution. This is why we chose to provide the algorithm with ~~fields taken from~~ Numerical Weather Prediction (NWP) forecast fields. These were acquired from the European Centre for Medium-Range Weather Forecasts (ECMWF) ERA5 forecasts initialised at 6 UTC and 18 UTC of each day (Hersbach et al., 2020). ~~These are~~ The ERA5 forecasts are a by-product of the reanalysis and more readily available for past time steps than the operational forecasts. They are different from ECMWF's Integrated Forecasting System (IFS) operational forecasts since they use more assimilated data in the initialisation time step. The forecasts are at a resolution of 0.25° and in 3 h steps. The data fields are interpolated to the observation time and FCI coordinates.

The variables needed are: horizontal wind speed (WSP) calculated from u- and v-component of the horizontal wind speed at 10 m above ground (U10, V10), ~~total column water vapour (TCWV)~~TCWV, surface air temperature at 2 m above ground (~~T2m)~~T2M), and surface air pressure (SP). The data were accessed via the Copernicus Climate Change (C3S) data store (Copernicus Climate Change Service and Climate Data Store, 2023). For testing and algorithm development, we used the ERA5 forecasts. In the later ~~operational~~ processing for the NWCSAF GEO software package, the operational ECMWF IFS forecasts at a resolution of 0.5° and 1 h steps will be used.

2.4 Aerosol Optical Thickness Climatology

One key parameter for the retrieval of TCWV over water is the aerosol optical thickness (AOT). As a first guess for AOT, we use a climatology at a 1° spatial resolution. It was built from monthly means of the Oxford-RAL Aerosol and Cloud (ORAC, Thomas et al. (2009)) aerosol optical properties data retrieved with Sentinel-3 Sea and Land Surface Temperature Radiometer (SLSTR) and ~~Enviromental~~ Environmental Satellite (ENVISAT) Advanced Along Track Scanning Radiometer (AATSR) between 2002 and 2022. These data were also accessed via the C3S data store (Copernicus Climate Change Service and Climate Data Store, 2019).

2.5 Reference Datasets~~and~~ , Match-up Analysis and Performance Indicators

In order to verify the credibility of the retrieved TCWV we need reference data within the field of view of FCI. There are four established sources of TCWV estimates: radiosondes, ~~ground based~~ ground-based GNSS meteorology, ~~microwave radiometers and~~ ground-based MWR, and ground-based direct sun-photometry. TCWV from NWP Reanalyses may also be used, but their coarse resolution cannot resolve the fine variabilities found in the WV field at the satellite-pixel scale. Reanalyses may be used to assess the stability of the dataset later on. Unfortunately, until the completion of this work, no ~~MTG-FCI data were~~ long-term record of FCI data was available in the final calibration. Because of this, we processed the spectrally representative ~~test~~ FCI data discussed above ~~. Nevertheless, the~~ and compared these against TCWV from the ERA5 reanalysis. The performance of our algorithm as well as the accuracy of our calculations, require testing on real data. Hence, we processed a 7-year matchup ~~dataset of OLCI observations and~~ database of OLCI Level 1b observations and MWR TCWV from the Southern Great Plains site of the Atmospheric Radiation Measurement ~~(ARM, Sisterson et al. (2016)) TCWV over their Southern Great Planes site. Additionally, a month of global~~ network (ARM) (Sisterson et al. (2016). Additionally, the set of 1800 OLCI-SLSTR ~~observations~~ swaths was processed with our algorithm ~~, also employing~~ (including the surface reflectance approximation from Sec. 3.4~~.~~). These were compared against reference TCWV data retrieved at sites of 1) the Aerosol Robotic Network (AERONET~~,~~) (Holben et al. (1998)), ~~the Atmospheric Radiation Measurement network (ARM,~~ 2) the ARM network (Turner et al. (2007); Cadeddu et al. (2013)) and ~~the SUOMINET (Ware et al., 2000).~~ 3) the SUOMINET network (Ware et al., 2000).

Prior to the analysis, OLCI swaths and ground-based network sites were collocated within 1 km and 30 minutes of a satellite overpass. A square of 11 by 11 pixels around the collocated center pixel ~~were~~ was taken into account. ~~These pixels then~~ Then, these pixels were screened for convergence~~of the algorithm~~, a cost-function below 1~~and cloud-cover using the Idepix cloud mask~~ , and cloud-screened with a buffer of 3 pixels ~~(3.6 km)~~ around the cloud mask, minimizing the effect of cloud

~~contamination on the TCWV quality assessment~~and cloud shadow contamination. Match-up cases with less than 95% valid pixels were rejected, the central 3 by 3 pixels had to be completely cloud-free.

Both in the assessment of assumptions and the assessment of TCWV quality, we use metrics. Their abbreviations are ~~following~~as follows: N is the number of matchups, MADP is the mean absolute percentage deviation, RMSD is the root mean square deviation, cRMSD is the centered RMSD (i.e., ~~bias corrected), R is the correlation,~~ the observation is corrected for the bias against the reference), R^2 is the Pearson correlation coefficient. ODR α and β are the orthogonal distance regression coefficients for the intersect and slope, respectively~~.~~, with equal weights for all data points.

3 Algorithm Description

3.1 Physical Background

The $\rho\sigma\tau$ WV absorption bands are due to the vibrational reaction in a gaseous water molecule ~~being~~ hit by a photon within a specific ~~wavelength range (roughly between 0.9 and 1.0 μm)~~range of wavelengths, see Fig. 1. ~~FCI features a "window" band with a nominal center wavelength of 0.865 μm (band 4, "VIS_08") and an "~~The absorption ~~" band with a nominal center wavelength of 0.914 μm (band 5, "VIS_09"). The spectral response functions (SRF) are also shown in Fig. 1.~~

~~Upper panel: The WV attenuation spectrum for an atmosphere with a low TCWV amount in orange (7.4 kg/m^2) and high TCWV amount in blue (57.6 kg/m^2) with data obtained from the Correlated K-Distribution Model Intercomparison Project (CKDMIP, Hogan and Matricardi (2020)). Center panel: The SRFs in the NIR part of the spectrum for the satellite instruments OLCI (blue) and SLSTR (orange). Lower panel: the SRFs in the NIR for FCI (red).~~

~~The absorption~~ of WV in ~~these spectral regions~~ this spectral region is weak compared to the ~~infrared region~~ TIR at, e.g., 6.7 or 7.3 ~~μm~~ µm (traditionally referred to as WV bands). Because of that, ~~a beam of sun light in the $\rho\sigma\tau$ range travels through the atmosphere and is reflected at the Earth's surface and travels trough the atmosphere again and may hit the sensor. This way, the~~ the whole column's content of atmospheric WV can be probed using the $\rho\sigma\tau$. While the signal within the absorption band decreases with WV content, an adjacent window band will be virtually unaffected by any change in WV amount along the line-of-sight (LOS). ~~However, the situation becomes more complex due to multiple scattering within the atmosphere. This photon scattering may lengthen or shorten the light path and thus affecting the amount of measured absorption.~~ FCI features a "window" band with a nominal center wavelength of 0.865 μm and an "absorption" band with a nominal center wavelength of 0.914 μm. The spectral response functions (SRF) are also shown in Fig. 1.

The overall strongest influence factor on the signal measured at the satellite sensor is the surface reflectance~~at the channel's wavelength, i.e., how much light is reflected at the surface~~ . This is also referred to as the surface spectral albedo (ALB) and is the ratio of outgoing irradiance against incoming irradiance at one specific wavelength. This depends on the type of surface covering (e.g., vegetation, sand, snow, etc.) and to some degree on the sun and viewing angles. For land cases the spectral albedo in the NIR is well above 0.3 and thus provides a strong signal relative to the absorption by WV. Over the majority of water surfaces, however, the surface reflectance is often well below 0.03. There is no direct way to measure this spectral albedo, hence an approximation is necessary. ~~This approximation is described in more detail in Sec. 3.4.~~

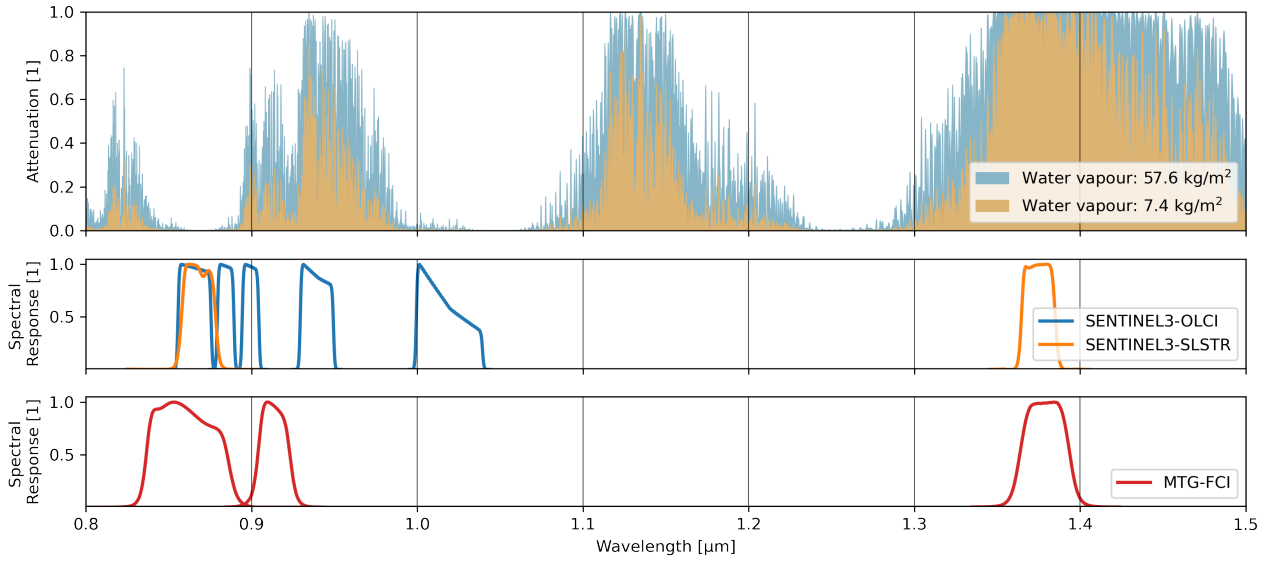

Figure 1. Upper panel: The WV attenuation spectrum for an atmosphere with a low TCWV amount in orange (7.4 kg/m^2) and high TCWV amount in blue (57.6 kg/m^2) with data obtained from the Correlated K-Distribution Model Intercomparison Project (CKDMIP, Hogan and Matricardi (2020)). Center panel: The SRFs in the NIR part of the spectrum for the satellite instruments OLCI (blue) and SLSTR (orange). Lower panel: the SRFs in the NIR for FCI (red).

A slightly less important effect comes from scattering aerosol layers below a certain level of aerosol optical thickness (AOT). In that case, the effective LOS is shortened by the higher aerosol layer, and since the humidity content on average is much lower in the higher troposphere, the absorption is decreased substantially. Over bright surfaces, this effect is much less important than over dark surfaces (Lindstrot et al., 2012). Since most natural surfaces over land are bright ~~at 0.9 μm, the amount of reflected light is high (albedos between 0.2 to 0.9) compared to the atmospheric reflectance. Then,~~ in the NIR, the shielding effect of an average aerosol layer is small (Diedrich et al., 2015).

Under most circumstances, this assumption is not valid for water surfaces, though. ~~On average, the reflectance of a water body in the NIR is well below 0.03. Thus~~Due to the low albedo, already slightly scattering layers of aerosol ~~in the troposphere~~ may create the effect described above~~and lead to an artificially "drier" signal~~. To a certain degree, this effect can be corrected for ~~, by simulating for~~ by simulating an aerosol layer with a specific ~~aerosol optical depth~~ AOT in the algorithm. However, for this, the effective height of the aerosol layer needs to be estimated ~~and this~~ which is a challenge in and of itself.

Another important aspect over water surfaces is ~~their~~ sunglint, i.e., the reflectance's dependency on wind-speed and viewing/solar geometry. High wind speeds ~~(rough surface) create a low reflectance peak (still higher than without sun glint)~~ create a rough surface with low reflectance peaks spread out over a range of observation geometry angles. ~~Low wind speeds(calm surface) create more of a peak with a much higher reflectance over a small range of an observation cone~~At lower wind speeds,

a calm surface results in a higher reflectance peak over a limited range of observation angles, similar to a mirror. In regions with strong sunglint, the relative influence of aerosol scattering is reduced.

Over both land and water surfaces, the atmospheric temperature profile and surface pressure play a lesser role due to temperature- and pressure-dependent line broadening (Rothman et al., 1998). For more detail, see In contrast to TCWV retrievals in the ~~IR~~TIR, the impact of the temperature profile is substantially lower but not negligible. The uncertainties due to a mis-characterised temperature profile are approximately 0.6 kg/m^2 and surface pressure at about 0.9 kg/m^2 (Lindstrot et al., 2012).

3.2 Forward Model

The first step in our framework is to run radiative transfer simulations (RTS) for a set of complete and comprehensive atmospheric, surface and geometric conditions as described in the previous section and summarised in Table 1 and 2.

For the simulation of top-of-atmosphere (TOA) reflectances we used the Matrix Operator Model (MOMo, ~~Fell and Fischer (2001); Hollst~~ Fell and Fischer (2001); Hollstein and Fischer (2012); Doppler et al. (2014)). These simulations are finally sorted into two land look-up-tables (LUT) for land surfaces and water surfaces, respectively. ~~The following variables and variable names are used within the algorithm and throughout this report: total column water vapour (TCWV), isotropic~~

Over land surfaces, the surface albedo (~~alb,$\rho_{BOA}(\lambda)$) , AOT, horizontal wind speed at~~ ALB) is defined as isotropic. Over water surfaces, the surface reflectance is estimated from the 10 m wind speed (WSP) ~~, surface pressure (SP), air temperature at 2 m~~ using Cox and Munk (1954). Standard atmospheric profiles were taken and adapted from Anderson et al. (1986) to provide the vertical distribution of temperature and humidity. The numbers refer to: 1. mid-latitude summer, 2. mid-latitude winter, 3. sub-Arctic summer, 4. sub-Arctic winter, 5. tropical. Based on the forecast surface air temperature (T2M) ~~, viewing/satellite zenith angle~~ and surface pressure (SP) the associated atmospheric profile group is chosen. The humidity profiles are scaled with TCWV. All simulations are done for a set of satellite zenith angles (SATZ), ~~satellite/viewing azimuth angle (SATA), sun /solar zenith angle~~ sun zenith angles (SUNZ) ~~, solar/sun azimuth angle (SUNA),~~ and relative azimuth (RAZI). ~~To avoid ambiguity in its definition we use Eq. 1:~~

$$RAZI = arccos(cos(SUNA) * cos(SATA) + sin(SUNA) * sin(SATA))$$

~~The measurements we use to retrieve TCWV is the window channel observation $nL_{TOA}(0.865\mu m)$ (a normalised radiance) and the absorption channel observation $\tau_{TOA}(0.914\mu m)$, a pseudo optical thickness, see Eq. 3. The normalised radiance is calculated following:~~

$$nL_{TOA}(\lambda) = \frac{L_{TOA}(\lambda)}{F_0(\lambda)}$$

~~where F_0 is the spectral solar irradiance.~~

~~The pseudo optical thickness is calculated following:~~

$$\tau_{pTOA}(\lambda) = -a - \frac{log(\frac{nL_{TOA}(\lambda)}{nL_{TOA^*}(\lambda)})}{\sqrt{AMF}} \cdot b$$

where AMF is the air mass factor, nL_{TOA} is the normalised radiance, $nL_{TOA}{}^{*}$ is the normalised radiance corrected for the influence of WV absorption, a RAZI is calculated from the satellite azimuth angle (SATA) and b are the so-called correction coefficients which may correct for a systematic bias discovered in a validation against reference TCWV observations. Preusker et al. (2021) have obtained these coefficients by minimizing the differences between simulated and measured OLCI observations using ARM-SGP.C1-MWR-TCWV as an input (see Preusker et al. (2021) for details). a and b for band 19 (at 0.9 μm) were estimated to be -0.008 and 0.984, respectively from the results shown in Sec. 4.1. For FCI another MWR TCWV reference (and associated TCWV observations) will be necessary, we intend to use the reference sites such as Meteorological Observatory Lindenberg – Richard Assmann Observatory (MOL–RAO) (Knist et al., 2022), the Cabauw Experimental Site for Atmospheric Research (CESAR) (Van Ulden and Wieringa, 1996) or ARM – Eastern North Atlantic (ENA) (Mather and Voyles, 2013) .

nL_{TOA} is calculated following Eq. 2 and $nL_{TOA}{}^{*}$ needs to be approximated using other available information (e.g., a climatology atlas, neighbouring window channels) . Here, we use a more elaborate technique, described in Subsection 3.4.

The AMF is calculated, following: sun azimuth angle (SUNA) following:

$$AMFRAZI = \frac{1}{cos(SUNZ)} arccos(cos(SUNA) * cos(SATA) + \frac{1}{cos(SATZ)} sin(SUNA) * sin(SATA)) \quad (1)$$

The aerosol mixtures and their optical properties have been calculated using the OPAC software package (Optical Properties of Aerosols and Clouds, Hess et al. (1998)). Within their documentation you can find details on the used aerosol mixtures for the two types chosen for the land and water surface simulations. Over land we used the aerosol mixture "continental average", over ocean we used the aerosol mixture "maritime clean". The standard atmospheric profiles used to set the vertical distribution of temperature and moisture were taken and adapted from Anderson et al. (1986). The numbers refer to: 1. mid-latitude summer, 2. mid-latitude winter, 3. sub-Arctic summer, 4. sub-Arctic winter, 5. tropical. The configurations In both cases, we simulated a homogenous aerosol layer between 700 to 1000 m height above ground with the specified AOT. An overview of the inputs and increments used for the simulations are listed is shown in Tables 1 and 2.

This

The observations we simulate are the normalised radiance in the window channel ($nL_{TOA}(0.865\mu m)$) and the pseudo optical thickness in the absorption channel ($\tau_{pTOA}(0.914\mu m)$). The normalised radiance is calculated as follows:

$$nL_{TOA}(\lambda) = \frac{L_{TOA}(\lambda)}{F_0(\lambda)} \quad (2)$$

where F_0 is the spectral solar irradiance.

The pseudo optical thickness τ_{pTOA} is calculated as follows:

$$\tau_{pTOA}(\lambda) = -a - \frac{log(\frac{nL_{TOA}(\lambda)}{nL_{TOA}{}^{*}(\lambda)})}{\sqrt{AMF}} \cdot b \quad (3)$$

Variable Name	~~Range~~ Increments and units
TCWV	0.1~~kg/m^2 to~~, 1.0, 5.0, 10., 25., 50., 75.0 kg/m^2
ALB	0~~to~~, 0.1, 0.3, 0.6, 1
T2M	standard atmospheric profiles 1 to 5*
SP	500~~hPa to~~, 650, 750, 850, 950, 1050 hPa
SUNZ	0~~° to~~, 10, 20, 30, 40, 50, 60, 70, 80, 90°
SATZ	0~~° to~~, 10, 20, 30, 40, 50, 60, 70, 80, 85°
RAZI	0~~° to~~, 18, 36, 54, 72, 90, 108, 126, 144, 162, 180°

Table 1. Land Surface Setup for MOMo. ~~TCWV = Total Column Water Vapour; alb = Surface albedo; T2M = Air Temperature at 2 m; SP = Surface Pressure at 2 m; SUNZ = Sun Zenith Angle; SATZ = Satellite Zenith Angle; RAZI = Relatie Azimuth Angle.~~ *Standard profiles from Anderson et al. (1986).

Variable name	Range and units
TCWV	0.1~~kg/m^2 to~~, 1.0, 5.0, 10., 25., 50., 75.0 kg/m^2
AOT	0.001, 0.1~~to 1.1~~, 0.3, 0.5, 0.7, 1.2 at 700 to 1000 m height
WSP	2~~m/s to~~, 3, 5, 10, 15 m/s
T2M	standard atmospheric profiles 1 to 5*
SP	950~~hPa to~~, 1000, 1050 hPa
SUNZ	0~~° to~~, 10, 20, 30, 40, 50, 60, 70, 80, 90°
SATZ	0~~° to~~, 10, 20, 30, 40, 50, 60, 70, 80, 85°
RAZI	0~~° to~~, 18, 36, 54, 72, 90, 108, 126, 144, 162, 180°

Table 2. Water Surface Setup for MOMo. ~~AOT = Aerosol Optical Thickness; WSP = Wind Speed.~~ *Standard profiles from Anderson et al. (1986).

where AMF is the air mass factor, $nL_{TOA}{}^*$ is the normalised radiance corrected for the influence of WV absorption, a and b are the so-called correction coefficients which may correct for a systematic bias discovered in a validation against reference TCWV observations.

The AMF is calculated as follows:

$$AMF = \frac{1}{cos(SUNZ)} + \frac{1}{cos(SATZ)} \tag{4}$$

Dividing through $\sqrt{AMF}$, the relationship between TCWV and τ_{pTOA} becomes more linear, reducing the number of necessary iterations in the inversion later on. $nL_{TOA}{}^*$ needs to be approximated using other available information (e.g., a climatology atlas, neighbouring window channels). Here, we use a more elaborate technique, described in Subsection 3.4.

Preusker et al. (2021) have obtained the correction coefficients a and b by minimizing the differences between simulated and measured OLCI observations using ARM-SGP.C1-MWR TCWV as an input (see Preusker et al. (2021) for details). For OLCI's version of this algorithm, a and b for band 19 (at 0.9 µm) were estimated to be -0.008 and 0.984, respectively, from the results shown in Sec. 4.1. For FCI, other MWR TCWV references will be necessary. We intend to use reference sites such as Meteorological Observatory Lindenberg – Richard Assmann Observatory (MOL–RAO) (Knist et al., 2022), the Cabauw Experimental Site for Atmospheric Research (CESAR) (Van Ulden and Wieringa, 1996) or ARM — Eastern North Atlantic (ENA) (Mather and Voyles, 2013).

The set of simulations is ~~then~~ sorted into a multi-dimensional look-up table (LUT). This LUT can then be used to simulate ~~an observation~~ a measurement ($\boldsymbol{y}$) for a given set of states ($\boldsymbol{x}$) and parameters ($\boldsymbol{p}$) using an interpolator. This is referred to as the forward model $\boldsymbol{F}$. With this forward model, we can estimate ~~an~~ a sensor's observation for a given set of states ~~, following~~as

follows:

$$\boldsymbol{y} = \boldsymbol{F}(\boldsymbol{x}, \boldsymbol{p}) + \epsilon \tag{5}$$

ϵ denotes the measurement and forward model error. The state vector of land consists of TCWV and ALB(0.865 µm), over water surfaces it consists of TCWV, WSP, and AOT. The parameter vector is composed of T2M, SP, SUNZ, SATZ and RAZI.

3.3 Inversion Using Optimal Estimation

Eq. 5 can be inverted ~~in order~~ to retrieve a state ~~describing an observationfrom a measurement by a sensor~~associated with an observation. There are various ways of performing ~~an~~ this inversion. We chose to follow the optimal estimation (OE) approach for atmospheric inverse problems described by Rodgers (2000). In essence, this inversion is based on the principle of minimizing the cost function $\boldsymbol{J}$ by iteratively changing the initial first guess of a state or the state of the prior iteration step. ~~$\boldsymbol{J}$ is calculated following:~~

$$\boldsymbol{J}(\boldsymbol{x}) = \frac{1}{2}(\boldsymbol{y} - \boldsymbol{F}(\boldsymbol{x}))^T {\boldsymbol{S_e}}^{-1}(\boldsymbol{y} - \boldsymbol{F}(\boldsymbol{x})) + \frac{1}{2}(\boldsymbol{x_a} - \boldsymbol{x})^T {\boldsymbol{S_a}}^{-1}(\boldsymbol{x_a} - \boldsymbol{x})$$

~~where $\boldsymbol{x_a}$ is the a priori state, $\boldsymbol{S_a}$ is the a priori error covariance matrix associated with $\boldsymbol{x_a}$ and $\boldsymbol{S_\epsilon}$ is the measurement error covariance matrix.~~

~~We assume the forward model and a priori knowledge to be bias-free and the inverse problem within the confines of the assumptions stated in previous Sections 3.1 and 3.2 to be near-linear. Then, we can use the Gauss-Newton approach to calculate the next step of the iteration $\boldsymbol{x_{i+1}}$ following:~~

$$\boldsymbol{x_{i+1}} = \boldsymbol{x_i} + ({\boldsymbol{S_a}}^{-1} + {\boldsymbol{K_i}}^T {\boldsymbol{S_\epsilon}}^{-1} \boldsymbol{K_i})^{-1} [{\boldsymbol{K_i}}^T {\boldsymbol{S_\epsilon}}^{-1}(\boldsymbol{y} - \mathbf{F}(\boldsymbol{x_i})) - {\boldsymbol{S_a}}^{-1}(\boldsymbol{x_i} - \boldsymbol{x_a})]$$

~~where $\boldsymbol{K}$ is the Jacobian which contains the partial derivatives of each measurement to each state at step i (i.e., $\boldsymbol{K_i} = \partial \boldsymbol{F}(\boldsymbol{x_i})/\partial \boldsymbol{x_i}$).~~ The iterative process is stopped if either the maximum number of allowed steps is reached or the following criterion is met by the retrieved state $\boldsymbol{x_{i+1}}$:

$$(\boldsymbol{x_i} - \boldsymbol{x}_{i+1})^T \hat{\boldsymbol{S}}_i^{-1} (\boldsymbol{x_i} - \boldsymbol{x_{i+1}}) \leq n \cdot \epsilon \tag{6}$$

where $\hat{\boldsymbol{S}}$ is the retrieval error-covariance~~. In this case we retrieve the true state $\boldsymbol{x}$. Under the assumption that the uncertainties of state, forward model and measurement are distributed Gaussian, we may calculate the associated uncertainty $\hat{\boldsymbol{S}}$ of $\boldsymbol{x}$:~~

$$\hat{\boldsymbol{S}} = ({\boldsymbol{S_a}}^{-1} + {\boldsymbol{K_i}}^T \cdot {\boldsymbol{S_\epsilon}}^{-1} \cdot \boldsymbol{K_i})^{-1}$$

, n is the number of state variables. More details on the process of ~~optimal estimation~~ OE within a TCWV retrieval framework can be found in Preusker et al. (2021) and El Kassar et al. (2021). ~~Factors such as the uncertainty of the prior knowledge or the measurement (e.g., the signal-noise-ratio; SNR)are taken into account. Such uncertainties~~ One crucial advantage of OE is the simultaneous retrieval of the associated uncertainty, the so-called retrieval error covariance matrix $\hat{\boldsymbol{S}}$.

$$\hat{\boldsymbol{S}} = ({\boldsymbol{S_a}}^{-1} + {\boldsymbol{K_i}}^T \cdot {\boldsymbol{S_\epsilon}}^{-1} \cdot \boldsymbol{K_i})^{-1} \tag{7}$$

Where, $\boldsymbol{S_a}$ is the a priori error covariance matrix associated with $\boldsymbol{x_a}$, $\boldsymbol{S_\epsilon}$ is the measurement error covariance matrix associated with $\boldsymbol{y}$ and $\boldsymbol{K}$ is the Jacobian which contains the partial derivatives of each measurement to each state at step i (i.e., $\boldsymbol{K_i} = \partial \boldsymbol{F}(\boldsymbol{x_i})/\partial \boldsymbol{x_i}$).

The covariances may either be set to values ~~which~~ that correspond to the actual covariances within a given variable. However, the ~~uncertainties~~ covariances may also be used as tuning parameters in order to make the algorithm lean more towards the measurement or more towards the prior knowledge ~~.~~ Rodgers (2000). Over land surfaces ~~,~~ we set the ~~apriori-uncertainty of the~~ a priori uncertainty of TCWV very high (16 kg/m^2) since the information content of the absorption band is high over bright surfaces. Over the ocean, the ~~apriori-uncertainty~~ TCWV a priori uncertainty was set much lower (2.5 kg/m^2). ~~Here the information content is much lower, due to the strong absorbance of the water body at the band wavelengths~~The ALB a priori uncertainty is set to 0.5, the WSP a priori uncertainty is set to 5 m/s, the AOT a priori uncertainty is set to 0.55. The corresponding covariances are the squared uncertainties.

The ~~retrieval procedure is as follows. First, FCI data are read in and then the necessary auxiliary fields (e.g., first guess TCWV,T2M, WSP) are read and interpolated to satellite resolution. As input for the prior knowledge and first guess we use the forecast at 6 or 18 UTC of the ECMWF ERA5 at a resolution of 0.25°. As a first guess for AOT we use the ORAC climatology at a 1° resolution. In the next step, the measurements (e.g. reflectances, , etc.) and the cloud mask are calculated. Then, a land and water processing mask is made. Here, pixels which are considered cloudy or which are closer to the night than the day, i.e., where the solar elevation angle is too slant (SUNZ $>$ 80°), are filtered out.~~ error covariance of τ_{pTOA} is estimated using the signal-to-noise-ratio (SNR), an interpolation-error (ϵ_{intp}),from the uncertainty in estimating $nL_{TOA}{}^*$) and AMF:

$$\boldsymbol{S_\epsilon}(\tau_{pTOA}) = \left(\frac{1}{SNR^2} + \frac{1}{SNR^2 + \epsilon_{intp}} \right) \cdot \frac{1}{AMF} \tag{8}$$

In 8, the two SNR-terms refer to the uncertainty of nL_{TOA}(0.914) and $nL_{TOA}{}^*$(0.914). For nL_{TOA}(0.865µm) the error covariance is simply $\frac{1}{SNR^2}$.

~~Subsequently, the interpolation is applied to the LUT to yield the simulated FCI measurements for the set of atmospheric, geometric and state variables for each pixel. These are compared against the real FCI measurements. Iteratively, the state is adjusted and again fed into the LUT-interpolation in order to move closer to the measurement within a pre-defined uncertainty and convergence criterion. Once this is reached, this state is passed out of~~ An additional metric this inversion technique provides is the so-called averaging kernel $\boldsymbol{A}$:

$$\boldsymbol{A} = \boldsymbol{G} \cdot \boldsymbol{K} = \frac{\partial \hat{\boldsymbol{x}}}{\partial \boldsymbol{x}} \tag{9}$$

where $\boldsymbol{G}$ is the Gain matrix, which contains the partial derivative of the true state $\partial \hat{\boldsymbol{x}}$ in relation to the ~~algorithm and these pixels are marked as converged. If a specific number of iterations is exceeded (8 over land, 6 over ocean), the algorithm stops and these pixels are marked as not-converged. Furthermore, an estimate of the associated uncertainty in the retrieved state is provided as part of the algorithm's output.~~ partial derivative of the measurement $\partial \boldsymbol{y}$. While the true state $\hat{\boldsymbol{x}}$ is unknown, the relative changes at each step quantify the sensitivity of $\hat{\boldsymbol{x}}$ towards changes in $\boldsymbol{y}$.

~~After the processing has finished for all pixels, data are only marked as valid if their cost is below a threshold (currently~~ ← The entries along the diagonal of $\boldsymbol{A}$ correspond to the state variables and show a range of values between 0 and 1. At 0,

the proportion of the retrieved state to $\hat{x}$ is lowest; the measurement did not contribute to the retrieval. At 1~~for land, < 1.5 for ocean) and if the convergence criterion has been met. This way, some cloudy pixels which have been missed by the cloud mask or pixels which contain a scattering aerosol layer may be filtered out. This is due to the fact that NIR-TCWV retrievals in the presence of elevated cloud or aerosol layers often lead to a substantial underestimation of TCWV, compared to the TCWV found in the prior /first guess. This leads to the cost function to become extremely high.~~

3.4 ~~Estimation of $nL_{TOA}{}^{*}$ with Principle Component Regression~~

~~The spectral albedo is the ratio of outgoing irradiance against incoming irradiance at one specific wavelength at a surface. Over clear, open ocean surfaces~~ , the ~~spectral albedos~~ proportion of the retrieved state to the true state is highest. Everything in between indicates that some improvement of the prior information about the state could be made using the measurement. The trace of AVK gives the degrees of freedom of the measurements.

3.4 Estimation of $nL_{TOA}{}^{*}$ with Principle Component Regression

For some surfaces (e.g., calm, clear water), the difference in spectral albedo between the window and absorption ~~bands are relatively close to each other (i.e., $nL_{BOA}(0.865) \approx nL_{BOA}(0.914)$)~~channel is small. Over most other surfaces, however, this is not the case. ~~The assumption, that the ratio of $nL_{TOA}(0.914\mu m)$ and $nL_{TOA}(0.865\mu m)$ would yield a reliable~~ Simply using nL_{TOA}(0.865µm) for $nL_{TOA}{}^{*}$ would yield an unreliable estimate of the ~~water vapour, would thus lead to substantial over and under-estimations, depending on the spectral slope.~~

~~In~~ pseudo optical depth τ_{pTOA}. Thus, in order to calculate ~~the pseudo optical depth at the absorption band~~ τ_{pTOA} we need an accurate estimate of the spectral slope between the window and the absorption channel. For satellite sensors such as MODIS or OLCI, the WV absorption bands have at least two accompanying window bands (i.e. at 0.865, 0.885, 1.02 or 1.2 ~~μm~~µm). FCI ~~does~~ and other future instruments do not have such ~~close additional window bands~~additional window channels close by. Hence, another technique to estimate the spectral slope is needed.~~The approach we chose to achieve this is based on the reconstruction of spectra from a~~ The principal component regression (PCR) facilitates the reconstruction of a continuous set of observations from few discrete data points. This approach is already used with reasonable success in the estimation of ~~BRDF~~ BRDFs and reflectance spectra within RTTOV ~~(Vidot and Borbás (2014))~~(Vidot and Borbás, 2014). Their approach was used as a ~~blue print~~ blueprint for our spectral slope estimation.

~~A spectrally high-resolved spectrum can be reconstructed from much fewer nodes with a so-called PCR. In order to do this, a collection of high resolved reflectance spectra with a high representativity is needed.~~ The ECOSTRESS spectral library version 1.0 provided by the United States of America Geological Service (USGS) is ~~such~~ a collection of spectral reflectances for individual materials and/or mixtures at a high spectral resolution (Meerdink et al., 2019). The library consists of spectra for ~~the following~~ a wide range of material groups: human-made, rock, soil, mineral, photosynthetic vegetation, non-photosynthetic vegetation, water (which includes fresh-water, ice, and snow). A small selection of these spectra is depicted in the upper part of Fig. 2, below, the SRFs of a selection of sensors are shown.

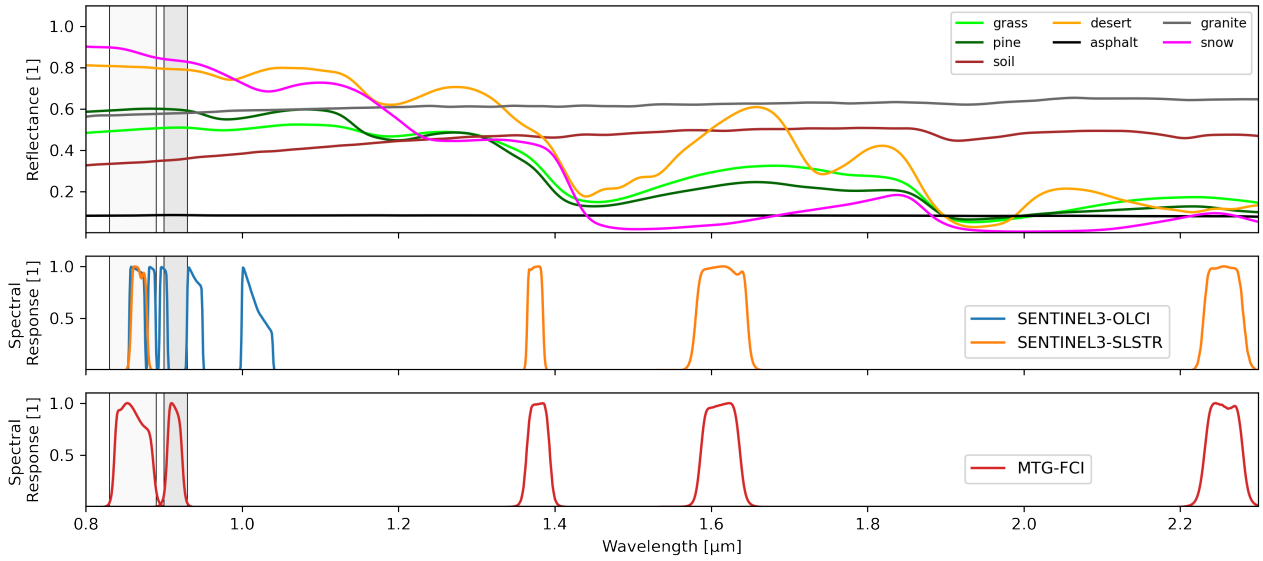

Figure 2. Upper panel: overview of a selection of surface reflectance spectra from Meerdink et al. (2019), the labels are representative and not the actual spectra designations. Central panel: the SRFs of OLCI (blue) and SLSTR (orange). Lower panel: the SRFs of FCI (red).

Only spectra ~~which were available~~ between 0.4 and 2.35 ~~μm~~ µm were taken into account and linearly interpolated to a spectral resolution of 0.001 ~~μm. Furthermore, we used sub-samples of each category, rather than the full collection to~~ µm. To avoid a sampling bias towards ~~rock, mineral and vegetation spectra~~a specific group of spectra, we used similarly sized subsets of each category. From this ~~collection, the principle~~ database, the principal components (the Eigenvectors, PCs) are calculated and sorted by their associated Eigenvalue.

~~Instead of using our~~ Instead of reconstructing spectrally high-resolved reflectances, we use the PCs to reconstruct ~~a spectrally high resolved spectrum we just reconstruct~~ the reflectance of two ~~bands: the NIR window band~~ channels: at 0.865 ~~μm and the NIR absorption band~~ µm and at 0.914 ~~μm~~ µm referred to as the *target*. Following the nomenclature of Vidot and Borbás (2014), $\boldsymbol{R}_{target}$ is the vector of reflectance spectra folded to the target SRFs, $\boldsymbol{c}_{win}$ is the regression coefficient vector (also referred to as ~~weigths~~weights) from the window ~~SRFs~~ bands and $\boldsymbol{U}_{target}$ is the matrix of the selected PCs of the high-resolution reflectance spectra, folded to the target SRFs.

$$\boldsymbol{R}_{target} = \boldsymbol{c}_{win}\boldsymbol{U}_{target} \tag{10}$$

Using the Moore-Penrose Pseudo inverse, the regression coefficient $\boldsymbol{c}_{win}$ follows:

$$\boldsymbol{c}_{win} = \boldsymbol{R}_{win}\boldsymbol{U}_{win}{}^{T}(\boldsymbol{U}_{win}\boldsymbol{U}_{win}{}^{T})^{-1} \tag{11}$$

An optimal configuration of the number of PCs and bands was then found by comparing different band combinations with several numbers of PCs. For this, we reconstructed all available spectra (which were used in the PCR) at the target bands from

the folded spectra at the window bands. Using this approach, the optimal configuration for ~~MTG-FCI~~ FCI was found with the use of five *window* bands (i.e., ~~no~~ negligible WV attenuation) in the VIS to SWIR (0.51, 0.64, 0.865, 1.61, 2.25 ~~μm~~µm) and only the first four PCs. We are able to reproduce the ~~"real"~~ actual surface reflectance at the absorption and window band with a bias of 0.0045 and 0.0038 and a RMSD of 0.016 and 0.02, respectively. ~~By folding~~ Folding the PCs to the SRFs of ~~another instruments makes~~ other sensors would make this matrix applicable to other ~~sensor~~ instruments with similar bands, as shown in Fig. 2. In order to estimate the spectral slope in the PCR, FCI's normalised radiances at the window channels need to be transformed into irradiance reflectances:

$$\rho_{TOA}(\lambda) = \frac{nL_{TOA}(\lambda) \cdot \pi}{cos(SUNZ)} \tag{12}$$

From the reconstructed surface reflectances we calculate the slope r:

$$r = \frac{\rho(0.914)}{\rho(0.865)} \tag{13}$$

This ratio is then multiplied with the $nL_{TOA}(0.865$~~μm) at 0.865μm~~ µm) in order to yield a more accurate estimate of $nL_{TOA}{}^{*}$ at the absorption band.

~~In order to estimate the spectral slope in the PCR, the normalised radiances at the window channels need to be transformed into reflectances:~~

~~$$\rho_{TOA}(\lambda) = \frac{nL_{TOA}(\lambda) \cdot \pi}{cos(SUNZ)}$$~~

The underlying assumption is that ~~within a window band it is valid that $\rho_{BOA}(\lambda) \approx \rho_{TOA}(\lambda)$ and the assumption of isotropic reflectance.~~ between 0.865 and 0.914 µm, atmospheric scattering and attenuation other than WV are nearly identical. Thus ~~$\frac{ALB(0.914)}{ALB(0.865)} \approx \frac{\rho_{0TOA}(0.914)}{\rho_{0TOA}(0.865)}$~~ holds true. Given a sufficiently bright surface and outside of the influence of thick, scattering layers (e.g., clouds, aerosols) or outside of very slant viewing geometries ($SATZ > 82°$), this is the case. Over water surfaces, the influence of scattering processes in the atmosphere is much stronger. Hence, the uncertainties over water pixels are higher. Furthermore, the influence of water constituents (e.g., sediment, pigments) on the water reflectance spectrum in the NIR has not been taken into consideration. The PCA training dataset almost exclusively consisted of terrestrial reflectances and only a few fresh water reflectances.

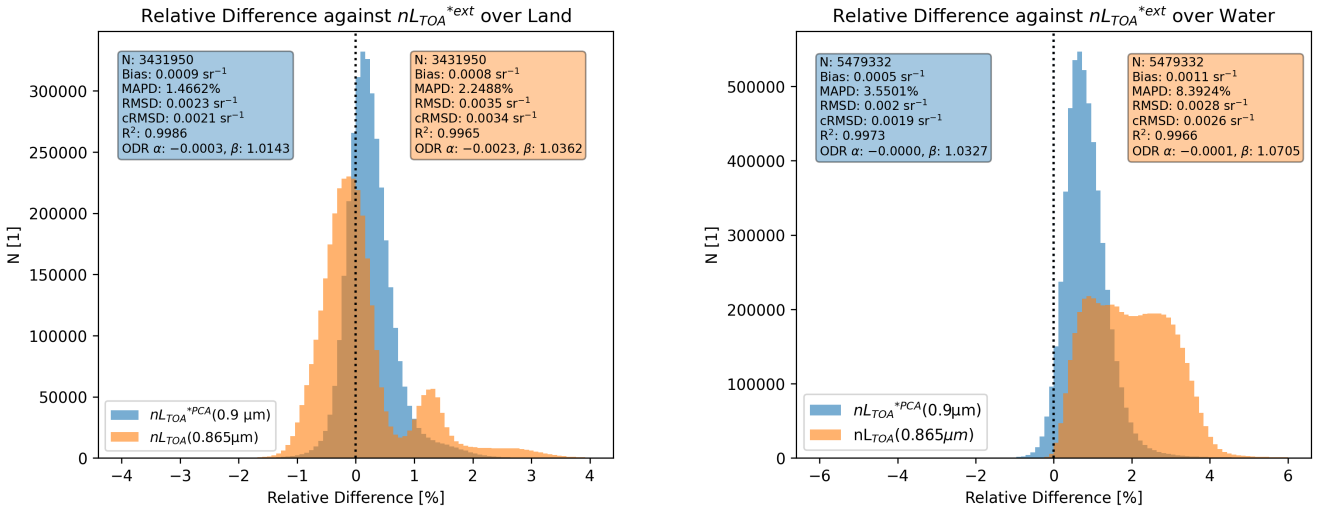

(a) Relative differences in $nL_{TOA}{}^{*}$ over land surfaces.

(b) Relative differences in $nL_{TOA}{}^{*}$ over ocean surfaces.

Figure 3. Relative differences between two proposed $nL_{TOA}{}^{*}$ against the extrapolated $nL_{TOA}{}^{*ext}$ as used in the COWa algorithm over land and water surfaces, respectively. The associated metrics in the corresponding colours are found in the top corners. The solid black line indicates 0% relative deviation.

Using ~~OLCI as a test-bed provides us a testing possibility: assessing~~ the OLCI/SLSTR synergy allows us to assess the performance of ~~our~~ the PCR to estimate τ_{pTOA} in comparison to directly using the window (~~$nL_{TOA}(0.865\mu m)$~~)nL_{TOA}(0.865 µm)) against a common reference. In the Copernicus Sentinel-3 OLCI Water Vapour product (COWa) algorithm, ~~the reference used for estimating~~ $nL_{TOA}{}^{*}$(0.9 ~~μm~~µm) is extrapolated ~~to the absorption band 0.9 μm~~ from the two ~~window bands~~ adjacent window bands at 0.865 and 0.885 ~~μm~~ µm (Preusker et al., 2021). For ~~the $\tau_{pTOA}(0.94\mu m)$ the absorption band surface reflectance~~ τ_{pTOA}(0.94µm), $nL_{TOA}{}^{*}$(0.94 µm) is interpolated from the two window bands 0.885 ~~μm~~ µm and 1.020~~μm~~µm. This is substantially closer to the ~~the~~ "real" surface reflectance than using ~~a~~ the PCR. Hence, we compare $nL_{TOA}{}^{*PCA}$(0.9 ~~μm~~µm) against $nL_{TOA}{}^{*ext}$(0.9 ~~μm~~µm) from the extrapolation using the two adjacent window channels. ~~The comparison shown in~~ For this and other comparisons, we calculated the relative difference in % by dividing the absolute difference (observation minus reference) by the reference multiplied by the factor 100. Fig. 3a and 3b ~~reveals~~ reveal that the vast majority of points lie close to 0 % line for both land and water pixels, albeit with a positive bias. In contrast, using the 0.865 ~~μm~~ µm normalised radiance by itself would yield much worse results. I.e., a strong bi-modal distribution over land and a weaker bi-modal distribution with a wide spread over water (see Fig. 3a and 3b).

On average, there is a small positive bias in $nL_{TOA}{}^{*PCA}$(0.9 ~~μm~~µm) both over land (+0.3%) and water (+0.8%). Over land pixels, the 98th percentile of the relative percentage deviation is 1.7% against the 2.6% when using ~~$nL_{TOA}(0.865\mu m)$~~ nL_{TOA}(0.865 µm) as $nL_{TOA}{}^{*}$. Over water pixels, the 98th percentile of the relative percentage deviation lies at 2.2%, whereas this value is 4% when using ~~$nL_{TOA}(0.865\mu m)$~~ $nL_{TOA}(0.865m)$ as $nL_{TOA}{}^{*}$. On average, an increase of 1% in $nL_{TOA}{}^{*}$(0.9 ~~μm~~µm) roughly translates to a 1.6% increase (~~i.e.,~~ approx. 0.9 kg/m^2) of TCWV estimate. A correction of this bias may

be possible, but since such an analysis cannot be carried out using FCI, we decided against it. Because the PCR performed ~~significantly~~ better than the window channel by itself, we decided to use $nL_{TOA}{}^{*PCR}$(0.9 ~~μm~~µm) to calculate τ_{pTOA} over both land and water surfaces. Despite the slight deviations, the PCR approach remains a good technique in order to reduce the impact of the spectral slope as much as possible.

This can also be demonstrated using a ~~test processing of TCWV~~ TCWV processed from a single day of OLCI/SLSTR observations. Here, we compared the retrievals from using each $nL_{TOA}{}^{*ext}$, $nL_{TOA}{}^{*PCR}$, and nL_{TOA}(0.865 ~~μm~~µm) to calculate τ_{pTOA} as input to the algorithm. In order to only see the influence on precision of TCWV, both datasets have been bias-corrected. The results are shown in Fig. 4. Over land surfaces, the bi-modal distribution in using nL_{TOA}(0.865 ~~μm~~µm) persists with large spread and systematic over- and ~~under estimations. Over~~ under-estimations. Over the ocean, the difference between the two approaches is even more pronounced. Both MAPD and RMSD indicate that using ~~the PCR to estimated $nL_{TOA}{}^{*}$ instead of simply the window channel~~ $nL_{TOA}{}^{*PCR}$ instead of nL_{TOA}(0.865 µm) for the calculation of τ_{pTOA} improves the retrieval substantially.

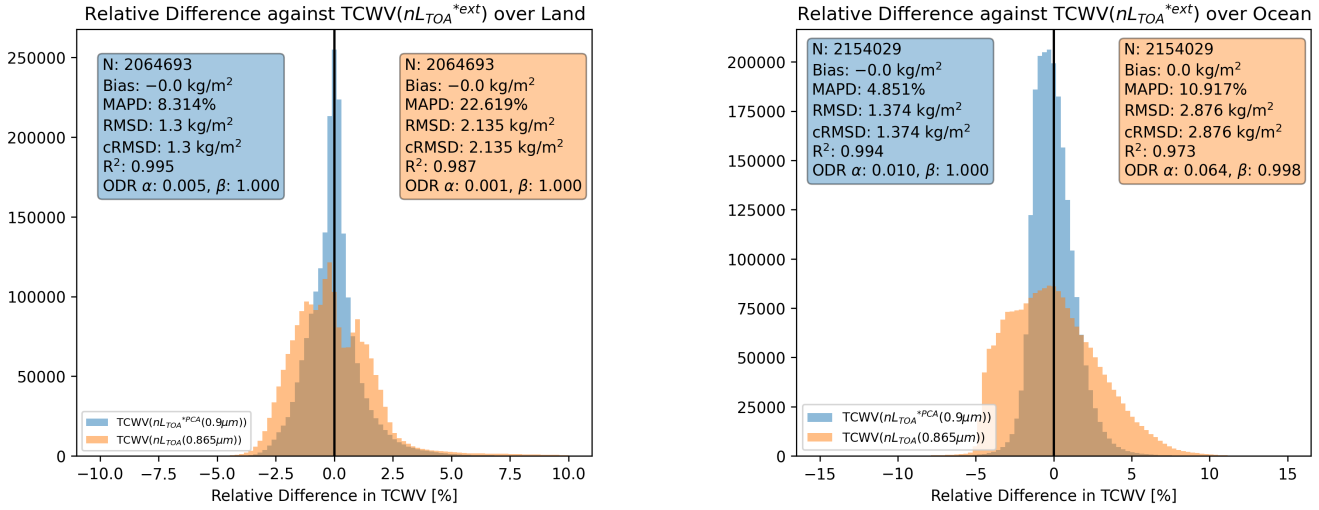

(a) TCWV using $nL_{TOA}{}^{*PCR}$from the PCR against the extrapolated $nL_{TOA}{}^{*}$(0.9 µm) over land pixels for a random subset of data in June 2021.

(b) Relative difference against $nL_{TOA}{}^{*}$(0.9 µm) from the PCR against the extrapolated $nL_{TOA}{}^{*}$(0.9 µm) over water pixels for a random subset of all data in June 2021.

Figure 4. Relative difference between TCWV retrieved with τ_{pTOA} calculated from extrapolated $nL_{TOA}{}^{*ext}$ and $nL_{TOA}{}^{*PCR}$ from the PCR in blue and τ_{pTOA} calculated from nL_{TOA}(0.865 ~~μm~~µm) in orange. The TCWV has been bias-corrected against the reference (TCWV using $nL_{TOA}{}^{*ext}$). The data are for a random subset of one day in June 2021. The associated metrics in the corresponding colours are found in the top corners. The solid black line indicates 0% relative deviation.

In very rare cases (<0.1%), there are large deviations (>5%). Upon visual inspection, these extreme deviations mostly occur along rivers, coasts, in high elevations or at the poles. We assign these cases to 1) ~~geolocation and unphysical spectral matches between OLCI and SLSTR~~unidentified clouds, 2) coastal ~~pixels with a mixed contribution~~ and inland water pixels

with mixed contributions by land and watersurfaces, 3) water-constituents changing the NIR reflectance of the water surface substantiallyor , 4) adjacency effects, the brightening effect of dark pixels by diffuse radiation from neighbouring bright pixels and 5) unidentified cloudsgeolocation and unphysical spectral matches between OLCI and SLSTR. Yet, these rare deviations are still lower than the extreme deviations found by using the window band at 0.865 µm µm itself.

3.5 Finalised Retrieval Framework

The retrieval procedure is as follows. FCI (or OLCI/SLSTR) radiometric and ancillary data are read and the necessary auxiliary fields (ECMWF forecast, AOT) are interpolated to satellite resolution. In the next step, the cloud mask and the measurements (e.g. reflectances, τ_{pTOA}, etc.) are calculated. A land and water processing mask is made. Pixels which are marked as cloudy or where $SUNZ$ is too slant ($> 80°$) are filtered out.

The inversion is run up until a pre-defined convergence criterion. Once this is reached, this state is passed out of the algorithm and these pixels are marked as converged. If the maximum allowed number of iterations is exceeded (6 over land, 8 over ocean), the algorithm stops, and these pixels are marked as not-converged. Furthermore, the estimate of the associated uncertainty in the retrieved state is provided as part of the algorithm's output.

After the processing has finished for all pixels, data are only marked as valid if their cost is below a threshold (currently <1) and if the convergence criterion has been met. With this, some cloudy pixels which have been missed by the cloud mask or pixels containing a thick and/or elevated aerosol layer may be filtered out. This is due to the fact that NIR-TCWV retrievals in the presence of elevated cloud or aerosol layers often lead to a substantial underestimation of TCWV, compared to the TCWV found in the prior/first guess. This leads to the cost function becoming extremely high.

4 Results

4.1 Sentinel3 OLCI and OLCI/SLSTR data

A first An initial test for our forward model as well as the inversion technique, was the application to an existing matchup database used for the validation and quality control of COWa. OLCI measurements were spatio-temporally collocated with the ARM network site Southern Great Plains (SGP) positioned in the Mid-West Midwest of the United States of America (USA). The dataset is limited to one location only and runs from 2016 until to 2023. Since SLSTR measurements are missing from this dataset, the approximation of ${nL_{TOA}}^{*PCR}$ in the absorption band using the PCA regression could not be done. Instead, we choose the same approach as COWa: extrapolate nL_{TOA} from band 17 (0.865 µmµm) and band 18 (0.885 µmµm) to band 19 (0.9 µmµm).

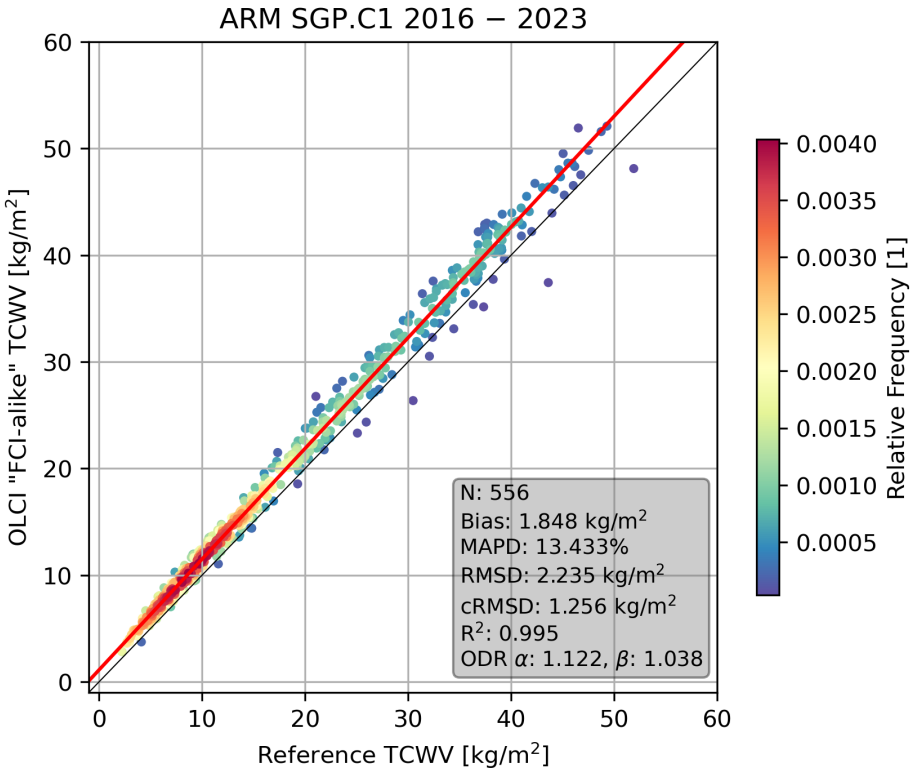

Figure 5. Comparison of S3OLCI "FCI-like" TCWV (using $nL_{TOA}{}^{*ext}$) against ARM TCWV at the SGP site, coloured with the relative frequency of occurrence. The solid black line presents the 1:1 line, the red line marks the ODR curve.

The analysis of the two-band ~~TCWV yielded~~ OLCI TCWV yields a strong correlation with a Pearson correlation coefficient of 0.995. The bias of 1.848 kg/m^2, orthogonal distance regression (ODR) coefficients, i.e., offset (α) and slope (β) of 1.122 and 1.038, respectively, indicate a slight wet bias. The cRMSD of 1.256 kg/m^2, RMSD of 2.235 kg/m^2 and MAPD of 13.433% still indicate slight spread.

In a next step, we ~~did a global processing~~ processed the global dataset of the OLCI-SLSTR synergy~~dataset for the month June in 2021.~~. This has been done in order to assess the quality of the two-band approach and the LUT-inversion in combination with the PCR approach to estimate τ_{pTOA}(0.9 ~~μm). Fig. **??** shows a global, daily composite from this dataset for 6th of June 2021. As a visual reference, the daily average of the ERA5 reanalysis as well as the COWa TCWV product are shown below. Since COWa was processed with the IdePIX cloudmask using an extra buffer of 2 pixels around each cloudy identified pixel, the grey areas are slightly larger in Fig. **??**. Significant features such as the dry airmasses at the poles and wet airmasses along the Inter-tropical Convergence Zone (ITCZ) exhibit very similar patterns.~~ µm).

~~Overview of different global TCWV products for the 6th of June 2021. Grey areas are due to cloud-cover or the retrieval not converging. Dark-grey indicates water surfaces, light-grey indicates land surfaces.~~

We used this global collection of TCWV to compare This TCWV was compared against three different reference observations of TCWV as wellnetworks. For this matchup analysis, we followed the same procedure as for the matchup analysis against the single ARM SGP stationmatchup procedure as before. The results of the comparison comparisons are depicted in Fig. 6a to 6d. Fig. 6a shows the positions of the ground-based reference sites with at least one valid matchup and with their associated networknameaccording to their network. For the ARM networkonly 2 stations , only 3 stations in North America were available for June 2021. Thanks to With AERONET and SUOMINETa wide , a wider range of different climate zones and atmospheric conditions can be coveredwithin only one month. The comparison of 281 714 valid matchups against AERONET 80 AERONET stations in Fig. 6b reveal reveals a wet bias of 3.121 2.84 kg/m^2, a MAPD of 36.705%18.36%, a RMSD of 3.906 3.6 kg/m^2, cRMSD of 2.35 2.21 kg/m^2, R^2 of 0.952 0.98, and ODR offset and slope of 1.558 and 1.107 0.56 and 1.13, respectively. The analysis results for 11 45 valid matchups against ARM MWR observations can be seen in Fig. 6c and show a slight wet bias of 1.23 0.33 kg/m^2, a MAPD of 6.98 6.64 %, a RMSD of 2.55 1.49 kg/m^2, a cRMSD of 2.24 1.46 kg/m^2, R^2 of 0.97 0.99, and ODR offset and slope of 1.79 and 0.980.33 and 1, respectively. In the comparison of 189 matchups against SUOMNINET GNSS TCWV 5439 matchups against 368 SUOMNINET stations, we find a wet bias of 2.006 1.38 kg/m^2, a MAPD of 41.243 16.03 %, a RMSD of 2.749 2.22 kg/m^2, a cRMSD of 1.879 kg/m^{2}1.75 kg/m^2, a R^2 of 0.96 0.98, and ODR offset and slope of 2.194 and 0.9830.65 and 1.04, respectively. Most SUOMINET stations are positioned in Central and North America.

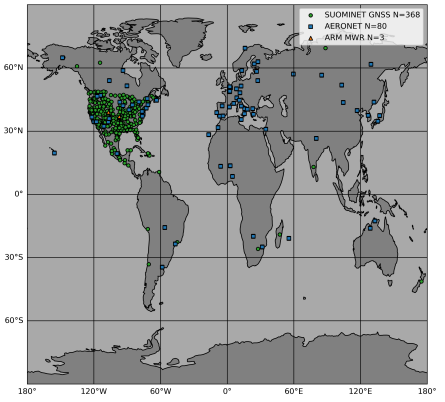

(a) Geographical distribution and their sum of all reference sites from which reference TCWV datasets are used in the matchup analysis.

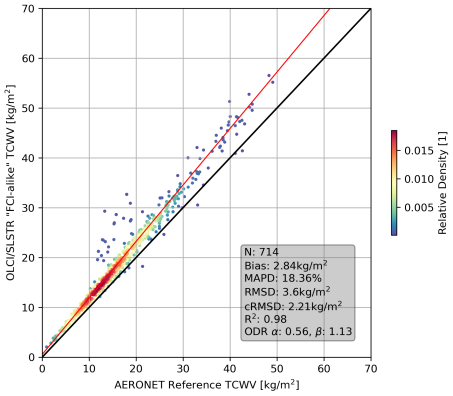

(b) Comparison of OLCI/SLSTR "FCI-like" TCWV against AERONET TCWV, coloured with the relative frequency of occurrence.

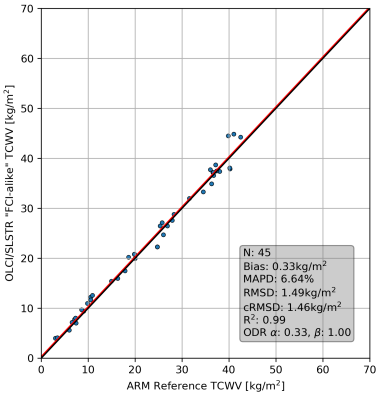

(c) Comparison of OLCI/SLSTR "FCI-like" TCWV against ARM at SGP.C1 TCWV.

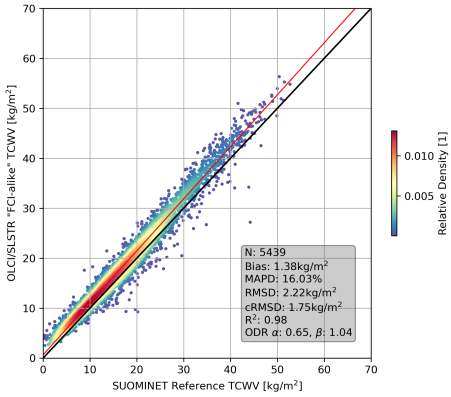

(d) Comparison of OLCI/SLSTR "FCI-like" TCWV against SUOMINET TCWV, coloured with the relative frequency of occurrence.

Figure 6. Matchup Analysis of OLCI/SLSTR "~~FCI-alike~~FCI-like" TCWV against globally distributed reference sites. This TCWV uses the PCR approach to estimate τ_{pTOA}. The solid black lines ~~presents~~ present the 1:1 line, and the red lines mark the respective ODR curves.

4.2 MTG-FCI Data

In order to test our algorithm with regard to future nominal FCI data, we applied the first prototype on test data provided by EUMETSAT. Since this dataset is still preliminary, this is neither a definitive nor ~~a~~ quantitative assessment. Rather, it serves to check the ~~processors~~ processor's performance with real data and check the product for any unexpected behaviour and/or defects. The data were gathered on the 13th of January 2024 at 11:50 UTC. The full-disk true colour RGB and ~~TCWV product processed~~ processed TCWV are depicted in Fig. 7a and 7b, respectively.

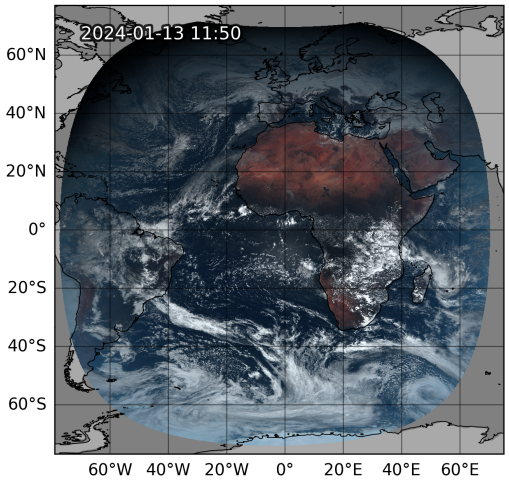

(a) FCI true colour composite.

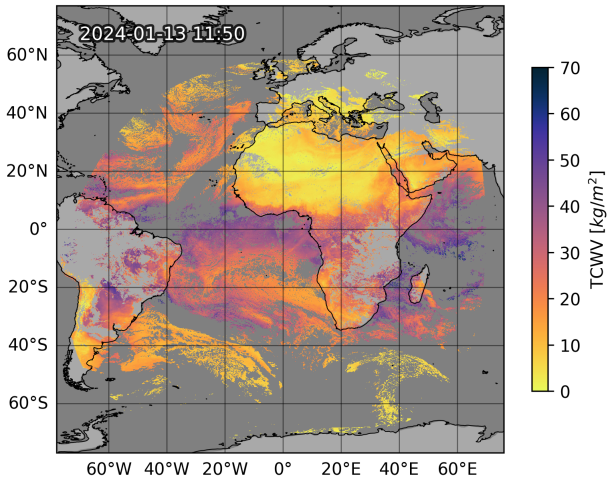

(b) Retrieved FCI TCWV field.

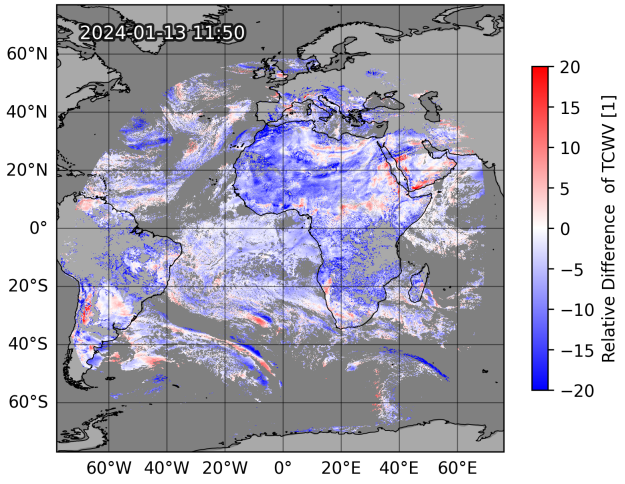

(c) Relative difference between FCI TCWV and ERA5 reanalysis TCWV.

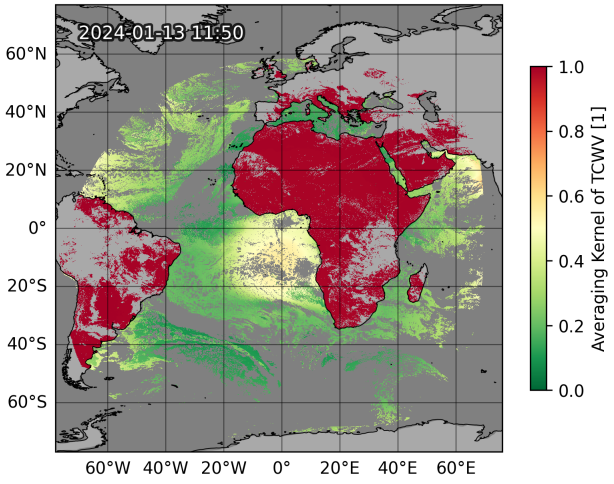

(d) AVK corresponding to the retrieved TCWV.

Figure 7. Fulldisk visualisation of TCWV and related products, processed from FCI data ~~aquired~~ acquired on 13 January 2024. Dark grey marks land surfaces, light grey marks water surfaces.

~~Areas identified as cloudy or which have too low sun or viewing zenith angles have not been processed. Pixels where the maximum number of iterations were exceeded, or the convergence criterion was not met or the cost function exceeded a threshold (0.5 over land, 1.0 over water) were masked out. Since the cloud-mask algorithm was set very loose, there are some cloud-contaminated pixels which have been processed with the algorithm.~~ In parallel processing, the running time of one full-disk scene ~~with on a machine~~ on a workstation with 64 GBs of RAM and a 12 core CPU lies below 5 minutes. In

single processing, the running time of a single chunk takes about 30 to 50 seconds. This includes ~~the~~ input/output operations, cloud-masking, PCR, and inversion.

~~Similar to Fig. ??, we~~ We can see lower TCWV values ~~at the higher latitudes , and much higher values~~ over mid to high latitudes and higher TCWV amounts all around the ITCZ in Fig. 7b. ~~Since we are in January, the ITCZ is positioned further south.~~ Arid regions such as the Sahara or the Arabian Peninsula are clearly visible. Europe also exhibits ~~quite low TCWVvalues~~low TCWV. Synoptic features such as bands of elevated moisture are ~~also~~ visible. Despite the wide range of viewing zenith and solar zenith angles and their implications for the line of sight, ~~we do not see any~~ there appears to be no influence on the TCWV product. Over Central Africa~~we can see that some clouds , which~~ , some clouds that are visible in the RGB ~~,~~ have not been detected by the ~~cloud-mask~~cloud mask. Such areas are also distinguishable by their decreased TCWV values compared to the surrounding areas. This underestimation due to clouds as well as the ~~more fine~~ finer details can be seen in a close-up of the scene in Fig. 8b. Because of the 1 km resolution of FCI's NIR channels, we can also detect meso- to mini-scale features such as smaller pockets of high moisture over the ITCZ or the mixing between dry and moist air masses. ~~Under certain circumstances closer~~ Closer to the shore, the TCWV field shows slight discontinuities between the water and ~~land-surface~~land surface. The water-pixels ~~very~~ close to the shoreline often show values which deviate a few percent ~~to~~ from the adjacent land-pixels~~, ~~; in most cases, there is an over-estimation. ~~This discontinuity is also visible in the TCWV field processed from OLCI and other NIR-TCWV retrievals.~~

At this stage, a rigorous quantitative validation of the TCWV product is not feasible, and our comparison against TCWV from the ERA5 ~~Reanalysis~~ reanalysis is not meant as such. ~~Rather, as~~ As a preliminary way to check the TCWV field for consistency, we ~~also~~ plotted the relative difference between the FCI TCWV and a collocated ECMWF ERA5 ~~Reanalysis~~ reanalysis TCWV, shown in Fig. 7c. This gives us a first impression if any artifacts or defects appear or if the algorithm works as intended~~and if there might appear some artifacts due to viewing- and or sun-geometry.~~ . The image in Fig. 7c is dominated by negative differences, which translates to a dry bias against the ~~Reanalysis~~ reanalysis TCWV. On average, FCI TCWV is approximately 10% drier than the ~~TCWV of the Reanalysis~~ reanalysis over land surfaces and 5% drier over water ~~surface.~~ ~~Furthermore~~surfaces. Furthermore, there are areas with positive and negative differences close to one another, often resembling a line, ~~i.e.~~e.g., over Northern Africa or over the South Atlantic. Fig. 7d depicts the ~~averaging kernel~~ AVK at each pixel. Over land, the value is close to 1 for most pixels since the forward model is very sensitive towards changes in the measurements. Over water, this value lies between 0 and 0.7. In areas of ~~light and or medium sun-glint, the averaging kernel~~ sunglint, the AVK ranges between 0.4 to 0.7~~(very central glint area)~~. In areas with low water-surface reflectance~~the averaging kernel~~ , the AVK approaches 0. ~~Where there is a higher AMF or higher values of~~ In areas with increased AMF and/or TCWV, the ~~averaging kernel~~ AVK is slightly higher between 0.1 to 0.3.

~~Comparison of FCI TCWV and OLCI/SLSTR "FCI-alike" TCWV for a close-up on the 27 June 2023 over Northern Mali.~~

To showcase FCI's spatial resolution, we ~~visually~~ compare a TCWV field from Sentinel3-A OLCI/SLSTR with ~~a zoomed-in look of a TCWV field from FCI 's test data~~ real preliminary calibrated FCI from the 27th June 2023 in Fig. 8. Both are processed with the algorithm described above. The temporal difference between the two fields is approximately 5 minutes. The scene is situated ~~over~~ in northern Mali in West Africa. ~~We can see the~~ The differences in viewing geometry are visible between

FCI and OLCI. In the true colour RGB of FCI, longer cloud shadows are visible, which are much smaller in the S3A-OLCI image, or their positions are shifted. The TCWV fields reveal a moist air mass in the South-East, while a drier air mass is positioned in the North-West. Consistent with the comparison against the ERA5 analysis, FCI TCWV is about 10% lower than OLCI TCWV. Hence, another colourmap-range is used in the FCI TCWV image(8b).

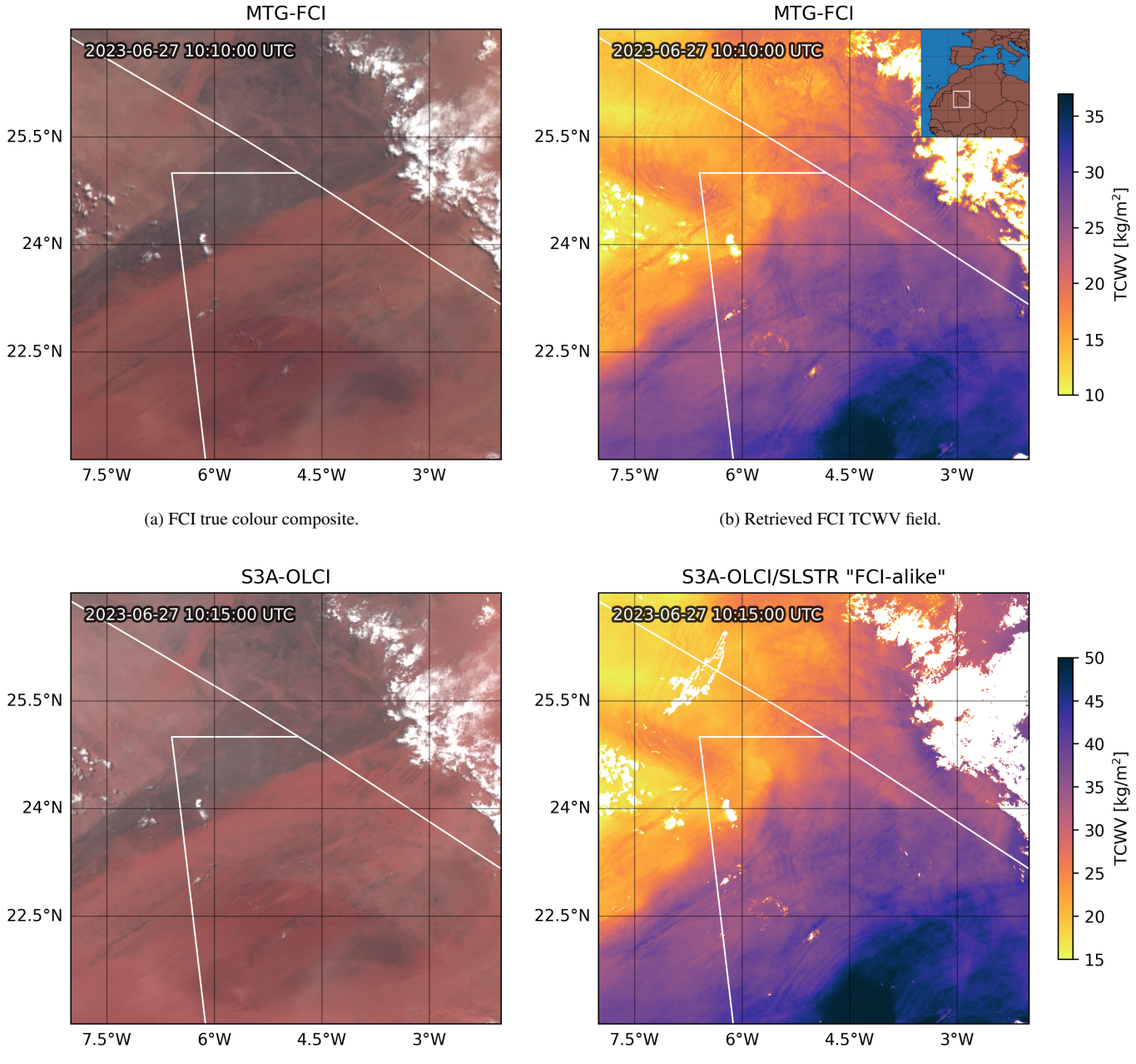

(a) FCI true colour composite.

(b) Retrieved FCI TCWV field.

(c) OLCI true colour composite.

(d) Retrieved OLCI TCWV field.

Figure 8. Comparison of FCI TCWV and OLCI/SLSTR "FCI-like" TCWV for a close-up on 27 June 2023 over Northern Mali.

FCI is capable ~~to reproduce~~ of reproducing the amount of detail found in the OLCI TCWV field: e.g., a dry line in the western half of the image (i.e., strong gradients in moisture between the air masses) or gravity waves in the southern half or north-eastern corner (local, wave-like peaks and trougths in TCWV). The positioning of features appears to be coherent

between the two sensors. Furthermore, we can see slight indications of ~~the~~ FCI's scan-lines in Fig. 8b. These are noisy pixels that follow lines ~~which~~ that run from East to West. The effect is more pronounced over water surfaces.

~~Overall the level of detail both products exhibit is high and gravity waves in the lower atmosphere are captured (local peaks and torughts in TCWV).~~ In both figures, the effect of unidentified cloud pixels on the TCWV is visible ~~: there, TCWV is underestimated and considerably drops compared to the surrounding clear-sky pixels~~through decreased TCWV at cloud edges. In contrast, there are some thin dust layers visible in the North-Western and Central-Eastern ~~part~~ parts of the RGBs, which do not show through in either of the TCWV ~~prodcuts~~products.

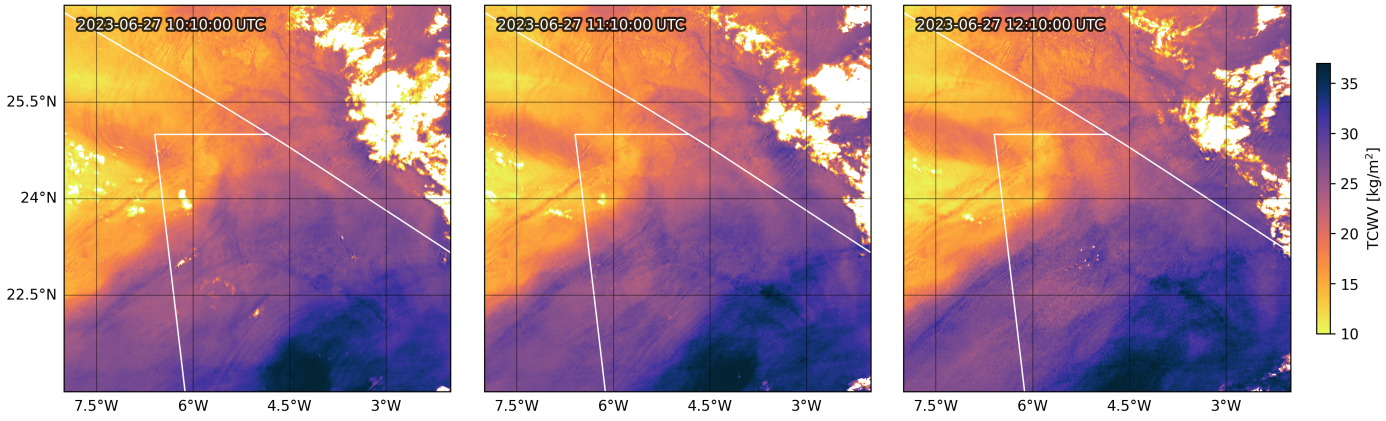

(a) (b) (c)

Figure 9. Time sequence of FCI TCWV shown in Fig. 8b with 1 hour between each frame.

To further highlight the potential of FCI TCWV observations for convective nowcasting purposes, we showcase the TCWV field from Fig. 8b again in 9 with the TCWV from two time steps later in Fig. 9a to 9c. The sequence demonstrates how one can track the propagation of the gravity waves and the north-western movement of the moist airmass along the moisture-front. The formation of what appear to be small updrafts or thermals is indicated by stark increases in TCWV from Fig. 9b to 9c. This results in a pattern similar to convective rolls shown in Carbajal Henken et al. (2015). There, in the lower center, at around 11:40 UTC first clouds are forming.

5 Discussion and Outlook

In the multi-annual validation against the reference ARM SGP TCWV dataset ~~, the "FCI-like"~~ (2016 – 2023), the OLCI 2-band TCWV shows a good performance with a bias of ~~of~~ 1.848 kg/m^2, RMSD of 2.235 kg/m^2, cRMSD of 1.256 kg/m^2, and high R^2 of 0.99. The wet bias ~~can~~ could be corrected following the procedure described in Preusker et al. (2021). In a comparison against their COWa algorithm applied to the same matchup dataset, they have a similar R^2 of 0.99 but a lower RMSD of 1.3

kg/m^2, which may well be attributed to both the use of an additional absorption band at 940 nm and initial τ_{pTOA}-correction. ~~The key performance indicators of the two-band approach still show robust retrieval results.~~

~~Upon visual inspection of the daily, global composites of TCWV, it can be seen that our algorithm reproduces both large-~~ ~~and small scale patterns down to a resolution of 1.2 km very well. The global comparison~~ Such a good performance against the reference ~~networks returned slightly lower performance indicators with R^2 between 0.95 to 0.97, bias between 1.23 to 3.12 kg/m^2, MAPD between 6.98 and 41.243 %, RMSD between 2.55 to 3.91 kg/m^{2}and cRMSD between 1.88 to 2.35 kg/m^2. The highest RMSD and bias is found in the comparisonagainst AERONET, which is most likely due to AERONET's dry bias (Pérez-Ramírez et al., 2014). Comparing the OLCI/SLSTR matchups against the multi-year matchup of only OLCI in, We observe a lower performance. This is due to much fewer matchups during a shorter time span and high geographic spread.~~ TCWV is promising, however, for this comparison, τ_{pTOA} has been estimated from two window bands (i.e., the same way COWa estimates τ_{pTOA}).

For ~~a rigorous validation, the assessment of a much longer time period will be essential. However, we can show that the PCRdoes not drastically reduce the algorithm's performance.~~

~~A crucial aspect that needs to be taken into account in the retrieval framework is the accurate estimation of surface reflectance in the absorption band. This is specific to the FCI instrument due to the absence of a second near-by window band (in contrast to OLCI). We implemented an approximation of the normalised radiance at the surface ($nL_{TOA}{}^*$) in the absorption band using a PCA regression.~~ FCI, the accuracy of τ_{pTOA} and subsequently TCWV mostly hinges on the PCR's ability to estimate the spectral slope. As shown in Figs. 3a and 3b~~The~~, the approximation shows a good performance against the next-best estimate, i.e., extrapolation from two adjacent window bands using OLCI measurements, and exceeds the performance of just using the window band at 0.865 ~~μm. Comparing $nL_{TOA}{}^{*PCR}$against $nL_{TOA}{}^{*ext}$reveals a bias of 0.001 sr^{-1} and RMSD of 0.002 sr^{-1}. The approximated~~ µm. Approximated $nL_{TOA}{}^*$ may deviate from the ~~"real"~~ reference $nL_{TOA}{}^*$ on average by 1.5 % over land and 3.5 % over water. In rare cases the ~~PCA regression failed.~~

~~The cases in which there is a very high deviation other than clouds mostly occur along rivers, coasts, in high elevations or at the poles.~~ PCR failed. We assume that there may be several processes at play ~~which~~ that require deeper investigations~~:~~

1. ~~water pixels with a complex composition (e.g. high loading of sediment or phytoplankton)~~
2. ~~sub-surface sea-floor reflections~~
3. ~~water pixels which actually contain sea-ice~~
4. ~~adjacency effects between surface interfaces (e.g. land-water, sea ice-water)~~
5. ~~snowy pixels which may be cloud-contaminated~~
6. ~~mis-alignment between OLCI/SLSTR, exacerbating all of the above~~

~~These effects may introduce over or underestimations of TCWV and are partially responsible for the discontinuities observable over lakes, rivers, shorelines. Discontinuities and overestimations of ocean pixels close to the shoreline or inland waters can also be observed in other NIR-TCWV products.~~

Such deviations introduce additional uncertainty in the initial estimate of and may explain some of the increased RMSD when compared to ARM using the extrapolated $nL_{TOA}{}^{*}$ in Fig. 5 and $nL_{TOA}{}^{*PCR}$ estimated from PCR in Fig. 6c. These types of mis-characterisations of the surface reflectance and the uncertainty of translate to a further . Miss-characterisations of the surface reflectance translate to an additional uncertainty of about 1 to 2 kg/m^2. Nevertheless, these initial results demonstrate that our approach is effective and advancing well towards an operational TCWV retrieval framework for FCI.

The global comparison against the reference networks returned slightly lower performance indicators with R^2 between 0.98 to 0.99, bias between 0.33 to 2.84 kg/m^2, MAPD between 6.64 and 18.36 %, RMSD between 1.49 to 3.6 kg/m^2, and cRMSD between 1.46 to 2.21 kg/m^2. The highest RMSD and bias are found in the comparison against AERONET, which is most likely due to AERONET's dry bias (Pérez-Ramírez et al., 2014). The OLCI/SLSTR matchup analysis shows a decreased performance against the multi-year matchup of only OLCI over ARM SGP. This is due to a reduced number of matchups over a shorter time span and a higher geographic spread. A more rigorous validation would require a longer time period. However, the aim of this assessment is to show that the PCR does not drastically reduce the algorithm's performance. The actual performance of FCI TCWV may deviate from these verification resultsusing reference TCWV datasets quite substantially, since the spectral characteristics and calibration are different from OLCI. E.g., FCI's window band at 0.865 μm is much wider and contains some residual WV absorption. Future validation studies have to be conducted for further characterization, which may also lead to a more elaborate correction for initial τ_{pTOA} estimation.

To assess the functionality of the current algorithm prototype, we applied it to the mtgt505 FCI L1c Level 1c test dataset provided by EUMETSAT. These are real FCI data captured on the 13th of January 2024. Conceptually, everything is in working order. The running times are close to or below the 5 minute 5-minute mark (FCI's nominal temporal resolution on a 2024 computer) and allow for a near-real-time and operational application of our TCWV product. For a fair comparison and accurate interpretation of TCWV field results, a good FCI cloud mask is essential.

algorithm. Full-disk comparisons show that the algorithm produces a sensible TCWV field. The relative difference between collocated ECMWF ERA5 Reanalysis reanalysis TCWV at 12 UTC and our TCWV product reveal that the majority of the field shows negative deviations, indicating a predominant dry bias. Furthermore, there are large-scale patterns of positive and negative deviations close to one another. Such patterns are to be expected in a comparison against model data and indicate that the model struggles with accurately capturing the advection of air masses in both space and time, while the observed TCWV fields might be closer to the actual state.

Using this initial comparison against ERA5 analysis we can deduce a FCI TCWV product reveals a systematic dry bias of approximately 8%. We see three probable reasons for this systematic dry bias: 1) the bias might be related to the preliminary calibration of the FCI data, 2) the PCR systematically over-estimates the surface reflectance at 0.914 μm µm and thus τ is too low and 3) undetected deficits in our LUTs. If this systematic bias persists in a future validation study and no underlying reason can be found, we may mitigate it using Preusker et al. (2021).

The analysis of the averaging kernel, a related OE output parameter, reveals by how far the retrieved state is influenced by the measurement. For FCI TCWV , over land this value is close to the empirical correction method described in Preusker et al. (2021) . Furthermore, there are large-scale patterns of positive and negative deviations close to one another. Such patterns are to be

expected in a comparison against model data and indicate that the model struggles with accurately capturing the advection of air masses in both space and time. The observed TCWV fields might be closer to the actual state. FCI's TCWV AVK of almost 1 ~~, indicating~~ indicates a high sensitivity to the measurement and only a ~~very~~ small contribution of ~~the~~ prior knowledge. This is also referred to as the algorithm being independent from the NWP input. This ~~property~~ is a key advantage of ~~the TCWV retrieved from the NIR~~ NIR-TCWV in contrast to other satellite-retrieved ~~sources of TCWV, which may either heavily depend on NWP inputs or provide a much coarser resolution. Over the majority of water surfaces , the averaging kernel is lower. This is mostly due to~~ TCWV. The decreased TCWV AVK over water surfaces is caused by the much lower ~~surface reflectance of the water surface resulting in a lower signal at the sensor. In some cases the~~ water surface reflectance in the NIR. In cases where the reflectance is close to 0, ~~making a retrieval of TCWV by differential absorption very~~ the retrieval is challenging. However, the OE ~~still provides~~ may still provide an update of the ~~prior~~ a priori TCWV field. ~~In such areas, the averaging kernel is close to 0. Over sun-glint dominated areas with higher surface reflectances, the averaging kernel lies between~~ Over sunglint, the AVKs above 0.4 ~~and 0.7, allowing for more accurate and independent TCWV retrievals in these regions.~~indicate that the retrieval is much more independent from the a priori and much more reliable.

Comparing OLCI and FCI TCWV up close, we can easily see that FCI TCWV matches the level of detail found in the OLCI TCWV product. ~~Patterns are well reproduced and areas affected by north-eastern winds are actually shifted towards the west, while patterns in the southern part of the image, where no strong winds can be found, remain stationary.~~ For scenes over Europe, ~~the resolution compared to OLCI~~ FCI's resolution will be slightly ~~decreased due to the curvature of the Earth.~~

~~The considerable under-estimation of TCWV in the presence of clouds is due to not-accounted for shortening of the photon paths and 3D effects. As a first measure, a better cloud mask is needed to filter out such pixels. At a later stage, such retrieved pixels may be used for an "above cloud" water vapour product. Such a product may then later be used for the detection of WV entrainment into the stratosphere, e.g. in the presence of overshooting tops (Setvák et al., 2008; Dauhut et al., 2018; Khordakova et al., 2022~~ ~~.~~ lower compared to OLCI's reduced resolution. Yet, FCI's resolution will be significantly higher than SEVIRI's. The stripes of enhanced noise ~~which~~ that run across the FCI TCWV image are caused by scan-lines of FCI. Similar scan-line artifacts are found in whisk-broom sensors, too, such as MODIS or VIIRS. Over land this ~~effect is not that pronounced,~~ is barely noticeable; however, over dark water pixels it is ~~more noticeable~~pronounced. This may change in future Level 1c processing versions.

The assessment exercises discussed above helped us identify several limitations and challenges regarding TCWV retrievals from FCI measurements. ~~One challenging factor is the spectral extrapolation using a reference calculated from the PCR. This challenge~~ The presence of clouds is visible as pixels with considerably lower TCWV than their surrounding. A robust cloud mask is needed to filter out such pixels. At a later stage, such retrieved pixels may be used for an "above cloud" water vapour product. Such a product may then be used for the detection of WV entrainment into the stratosphere, e.g., in the presence of overshooting tops (Setvák et al., 2008; Dauhut et al., 2018; Khordakova et al., 2022).

While over the vast majority of surface types, the PCR yields reliable $nL_{TOA}{}^{*}$, in some cases it deviates far from the reference. This may be addressed by ~~1)~~ extending the training ~~reflectance spectra dataset the PCA is built fromwith exemplary spectra from different water bodies (i.e. fresh-water, chlorophyll dominated, sediment dominated, etc.) or 2) a dedicated water~~

~~PCA or 3)a dedicated inland-water LUT, containing all the aforementioned parameters. Another fundamental~~ dataset the PCs are calculated from.

Currently, we use a fixed aerosol type, height, and thickness. Under conditions violating these assumptions (e.g., a strong dust outbreak), retrieval quality would be decreased. We consider to simulate for additional aerosol mixtures and aerosol layer heights. Furthermore, using AOT forecasts from the Copernicus Atmosphere Monitoring Service (CAMS) could improve the retrieval. Another issue is that over water surfaces, the inversion framework is under-determined: a measurement vector with only two elements (~~nL_{TOA}(0.865)~~nL_{TOA}(0.865 µm), τ_{pTOA}(0.914 ~~μm~~µm)) is opposed by a state vector with ~~at least~~ three elements (TCWV, AOT, WSP). Outside of ~~sun-glint areas~~ sunglint, the influence of the wind speed is marginal, and AOT mainly increases the TOA signal (and thus the forward model is not sensitive to changes of the windspeed)~~and inside sun-glint the surface signal is much stronger and the~~ , and inside sunglint the influence of a thin layer of aerosol ~~reduced (similar to land surfaces)~~is reduced. Because of that, the ~~information-content~~ information content is relatively balanced, and the impact is slightly reduced. ~~However,~~ Nevertheless, over water surfaces, adding an additional third channel to the ~~water-part of the algorithm (e.g.0.550 μm~~ measurement vector (e.g., 0.51 or 1.61 ~~μm) may improve~~ µm) may also improve the performance.

With FCI, we are able to monitor the temporal evolution of these small-scale patterns at a resolution similar to OLCI's. This allows for the tracking of large- and small-scale dynamics before, during, and after convective development. Such features and their changes (e.g., convergence zones, convective rolls, deepening boundary layers) contain potential information for nowcasting purposes. Furthermore, the patterns observed in FCI TCWV may also be tracked and used to retrieve lower level atmospheric motion vectors (AMV).

Our framework may be adapted to provide accurate TCWV retrievals for other sensors featuring at least two channels in and around the $\rho\sigma\tau$ band. The National Oceanic and Atmospheric Administration (NOAA) is commissioning GeoXO Imager (GXI), the successor to the Advanced Baseline Imager (ABI) on the ~~instruments on the~~ Geostationary Operational Environmental Satellite - 3rd generation (GOES)~~which~~ , which will include a WV absorption band in the ~~NIR~~ $\rho\sigma\tau$ region (Lindsey et al., 2024). Another future instrument soon to be launched into a polar orbit is METImage, flying onboard EUMETSAT's Meteorological Operational satellite second generation A (METOP-SG-A) (Phillips et al., 2016). METImage will enable NIR TCWV with a spatial resolution of 500 m and global coverage every day. METImage will also provide O2A band measurements (around 0.76 µm), which can be used to reduce ambiguity due to shielding of cirrus or elevated aerosol layers. A NIR TCWV product from METImage may then be used in advanced synergies with sounders such as Infrared Atmospheric Sounder Interferometer - New Generation (IASI-NG), which will also be flying on METOP-SG-A. IASI-NG is the successor of IASI, which provides all-sky temperature and humidity profiles with a slightly lower accuracy in the presence of clouds (Müller, 2017).

Furthermore, the Infrared Sounder (IRS) will be operating on MTG-S1, MTG-I1's sister satellite, ~~which covers~~ and will cover the same field of view as ~~MTG-FCI~~FCI. This will enable a synergy between TCWV from FCI and the IRS humidity profile product. NIR TCWV could very well complement profile soundings for both IASI-NG and IRS: one ~~short-coming~~ shortcoming of these retrievals is their low or missing sensitivity to the lowest layers of the troposphere (below 1-2 km). Furthermore, their spatial resolution is in the order of tens of km, often insufficient ~~in~~ for assessing small-scale weather patterns. A high-spatial

resolution NIR TCWV product, sensitive to the whole column of air, could complement such sounding products perfectly, albeit in the absence of clouds. A synergy could consist of an updated ~~layer-product~~ layer product or a product ~~which~~ that provides the moisture content of the lowest levels of the troposphere. Such synergy products could provide crucial insights ~~of~~ into the meteorological conditions, such as the atmospheric instability, and improve the potential for the prediction of severe weather.

~~Yet, a more zoomed-in look into a FCI TCWV field obtained from real data reveals that FCI TCWV alone is capable of observing small-scale patterns also visible in an OLCI/SLSTR TCWV field. The capability of seeing such small-scale WV features (e.g. convergence zones, convective rolls, deepening boundary layers) emphasizes the potential of an operational FCI NIR TCWV product for nowcasting purposes. Last but not least, and to further highlight the potential of MTG-FCI based WV observations for convective nowcasting purposes, we showcase the TCWV field from Fig. 8b again together with the TCWV from two time steps later in Fig. 9a to 9c. The sequence demonstrates, how one can track the propagation of the gravity waves and the north-western movement of the moist airmass along the moisture-front. What is more compelling, is, that we can detect the formation of small updrafts or thermals indicated by the stark increases in TCWV from 9b to 9c. This results in a pattern similar to convective rolls shown in Carbajal Henken et al. (2015). In the lower center, at around 11:40 UTC first clouds are forming.~~

~~Time sequence of FCI TCWV shown in Fig. 8b with 1 hour between each frame.~~

~~Time sequence of FCI TCWV shown in Fig. **??** to **??** with 10 minutes between each frame, leading up to cloud formation at 11:40 UTC. The range of the colormap has been further adjusted to show more detail. The cloud formation is visible in RGBs (not shown) and be distinguished by the sudden appearance of clouds (i.e., white spots) in **??** to **??**.~~

~~An even closer look at the time shortly before these clouds forming, FCI NIR TCWV reveals even more intricate details in Fig. 9. The pattern structure shows what are assumed to be individual convective cells growing in depth, shortly before cloud formation.~~

~~This case highlights both the remarkable large-scale and small-scale WV features that will be observable with FCI. FCI will not only provide a snapshot of convective cloud formation but a steady stream of data. These show how the TCWV field changes in clear-sky regions around clouds or before the onset of cloud formation, given the presence of sufficient daylight. With real FCI data we can monitor the temporal evolution of TCWV fields, allowing us to track and comprehend both large-scale and small-scale dynamics before, during and after convective development. Images such as Fig. 9 could be provided by MTG-FCI way in advance of the formation of the first clouds and could help to pin-point areas of local convergence and increased low level moisture for nowcasters. Above that, the spatio-temporal resolution of MTG-FCI may even provide deeper insight into the conditions of severe storm formation.~~

6 Conclusions

Leveraging our expertise in ~~Total Column Water Vapour~~ total column water vapour (TCWV) retrievals from Near-Infrared (NIR) measurements for various satellite-based passive imagers, we developed a new retrieval framework for the new Me-

teosat Third Generation Flexible Combined Imager (MTG-FCI) measurements. ~~Although the latest calibrated Level 1 FCI data were not available by the time this work was completed, we utilized both OLCIdata and an initial version of L1~~ The use of OLCI/SLSTR synergy "FCI-like" data proved valuable for establishing and validating an adapted TCWV retrieval framework for MTG-FCI~~data, alongside reference TCWV data from other sources, to assess the performance of this two-band NIR-TCWV retrieval framework.~~ . It offers a realistic and reliable testbed that supports algorithm development ahead of the availability of a sufficiently long and calibrated FCI data record. Key challenges, such as the surface reflectance treatment in the WV absorption band, can be addressed in preparation for the large-scale application of the retrieval to FCI data.

The evaluation exercises highlight the robustness of the retrieval framework and helped identify specific challenges and limitations related to the MTG-FCI instrument, which can be further addressed with fully calibrated FCI data in the near future.

As the successor to MSG-SEVIRI, MTG-FCI boasts extended observational and spectral capabilities that promise significant advancements in weather and climate research and applications, particularly in the monitoring and study of atmospheric TCWV amounts and dynamics. Notably, FCI is the first geostationary satellite instrument with measurements in the NIR $\rho\sigma\tau$ WV absorption band. While SEVIRI TIR measurements allowed ~~to derive~~ for to derivation of information on WV amounts mainly in higher parts of the troposphere, the FCI NIR WV absorption measurements exhibit the greatest sensitivity to WV amounts near the surface. This enables accurate and high temporal resolution observations of changes in moisture content in the lower troposphere. Consequently, these novel and comprehensive TCWV observations will enhance the (real-time) monitoring of atmospheric moisture distributions in the boundary layer, their evolution, and associated meteorological phenomena across regional to continental scales, with the potential to significantly advance nowcasting techniques.

Code availability. After further refinement, the code will be made available via the NWCSAF GEO software package via: https://www.nwcsaf.org/nwc/geo-geostationary-near-real-time-v2021

Data availability. OLCI/SLSTR data obtained from here: EUMETSAT. ERA5 data obtained from here: Copernicus Climate Change Service and Climate Data Store (2023). Satellite AOT obtained from Copernicus Climate Change Service and Climate Data Store (2019)

Author contributions. Conceptualization, J.E.K., C.C.H., R.P.; methodology, J.E.K., C.C.H., R.P.; software, R.P., J.E.K.; validation, J.E.K.; formal analysis, J.E.K., C.C.H., R.P.; investigation, J.E.K., C.C.H., R.P.; resources, J.E.K., C.C.H., R.P., X.C., J.F.; data curation, J.E.K.; writing—original draft preparation, J.E.K.; writing—review and editing, J.E.K., C.C.H., R.P., X.C., P.R.; visualization, J.E.K.; supervision, R.P.; project administration, X.C., P.R.; funding acquisition, J.E.K., C.C.H., R.P., P.R., J.F..

Variable	Definition/ Explanation
$\boldsymbol{A}$	averaging kernel matrix
a	τ_{pTOA} correction offset
b	τ_{pTOA} correction slope
ALB	surface albedo, i.e., surface irradiance reflectance
AMF	air mass factor
AVK	averaging kernel
$\boldsymbol{c_{win}}$	regression coefficient vector
$\boldsymbol{\epsilon}$	forward model uncertainty
$\boldsymbol{\epsilon_{intp}}$	$nL_{TOA}{}^{*}$ approximation uncertainty
$\boldsymbol{F}$	forward model
F_0	spectral solar irradiance
$\boldsymbol{G}$	gain matrix
$\boldsymbol{K}$	jacobian matrix
λ	wavelength
L_{TOA}	top-of-atmosphere radiance
nL_{TOA}	normalised top-of-atmosphere radiance
$nL_{TOA}{}^{*}$	normalised top-of-atmosphere radiance corrected for WV attenuation
$nL_{TOA}{}^{*ext}$	$nL_{TOA}{}^{*}$ estimated from extrapolation of window bands
$nL_{TOA}{}^{*PCR}$	$nL_{TOA}{}^{*}$ estimated from principle component regression
$\boldsymbol{p}$	parameter vector
$\boldsymbol{r}$	spectral slope
$\boldsymbol{R_{target}}$	reflectance vector of target
$\boldsymbol{R_{win}}$	reflectance vector of window channels (source)
ρ	irradiance ratio reflectance
ρ_{TOA}	irradiance ratio reflectance at top-of-atmosphere
$\hat{\boldsymbol{S}}$	retrieval error covariance matrix
$\boldsymbol{S_a}$	a priori state error covariance matrix
$\boldsymbol{S_\epsilon}$	measurement error covariances matrix
SATA	satellite azimuth angle
SATZ	satellite zenith angle
SNR	signal to noise ratio
SUNA	sun azimuth angle
SUNZ	sun zenith angle
τ_{pTOA}	pseudo optical thickness
$\boldsymbol{U_{target}}$	principle components folded to target band spectral response functions
$\boldsymbol{U_{win}}$	principle components folded to window band spectral response functions
RAZI	relative azimuth angle
RAZI	relative azimuth angle
$\boldsymbol{x}$	state vector
$\hat{\boldsymbol{x}}$	true state vector
$\boldsymbol{x_a}$	a priori state vector
$\boldsymbol{x}$	state vector
$\boldsymbol{y}$	measurement vector

Table A1. List of variables and their respective explanations.

Competing interests. The authors declare no conflict of interest.

Acknowledgements. This research has been partially funded by the Satellite Application Facility in Support to Nowcasting and Very Short Range Forecasting (NWCSAF) of the European Organisation for the Exploitation of Meteorological Satellites (EUMETSAT) through the Associated Visiting Activity NWC_AVS23_01, by EUMETSAT COWa Contract EUM/CO/18/4600002115/EJK, by EUMETSAT FRAME Contract EUM/CO/24/4600002869/JoSt and by the Deutsche Forschungsgemeinschaft (DFG, German Research Foundation) - Project number: 320397309 (TP2 QPN) within FOR 2589 "Near-Realtime Quantitative Precipitation Estimation and Prediction" (RealPEP). We acknowledge the legacy and software of COWa that went into this algorithm, supported by the Remote Sensing Products (RSP) division of EUMETSAT. We thank NWCSAF and EUMETSAT for the provision of preliminary MTG-FCI data. We thank all researchers and staff for establishing and maintaining the AERONET Sites, SUOMINET Sites and ARM Sites used in this investigation.

References

Ackerman, S., Frey, R., Strabala, K., Liu, Y., Liam, G., Baum, B., and Menzel, P.: Discriminating Clear-Sky from Cloud with MODIS—Algorithm Theoretical Basis Document (MOD35), ATBD Reference Number: ATBD-MOD-06, Goddard Space Flight Center, Tech. rep., NASA, accessed: 2024-08-29, 2002.

Albert, P., Bennartz, R., Preusker, R., Leinweber, R., and Fischer, J.: Remote Sensing of Atmospheric Water Vapor Using the Moderate Resolution Imaging Spectroradiometer, http://www.cloudmap., 2005.

Allen, M. R. and Ingram, W. J.: Constraints on future changes in climate and the hydrologic cycle, Nature, 419, https://doi.org/10.1038/nature01092, 2002.

Anderson, G. P., Clough, S. A., Kneizys, F. X., Chetwynd, J. H., and Shettle., E. P.: AFGL atmospheric constituent profiles (0-120km), AFGL-TR-86-0110 (OPI), 1986.

Benevides, P., Catalao, J., and Miranda, P. M.: On the inclusion of GPS precipitable water vapour in the nowcasting of rainfall, Natural Hazards and Earth System Sciences, 15, 2605–2616, https://doi.org/10.5194/nhess-15-2605-2015, 2015.

Bennartz, R. and Fischer, J.: Retrieval of columnar water vapour over land from backscattered solar radiation using the medium resolution imaging spectrometer, Remote Sensing of Environment, 78, 274–283, https://doi.org/10.1016/S0034-4257(01)00218-8, 2001.

Cadeddu, M. P., Liljegren, J. C., and Turner, D. D.: The atmospheric radiation measurement (ARM) program network of microwave radiometers: Instrumentation, data, and retrievals, Atmospheric Measurement Techniques, 6, 2359–2372, https://doi.org/10.5194/amt-6-2359-2013, 2013.

Carbajal Henken, C., Dirks, L., Steinke, S., Diedrich, H., August, T., and Crewell, S.: Assessment of sampling effects on various satellite-derived integrated water vapor datasets using GPS measurements in Germany as reference, Remote Sensing, 12, https://doi.org/10.3390/rs12071170, 2020.

Carbajal Henken, C. K., Diedrich, H., Preusker, R., and Fischer, J.: MERIS full-resolution total column water vapor: Observing horizontal convective rolls, Geophysical Research Letters, 42, 10 074–10 081, https://doi.org/10.1002/2015GL066650, 2015.

Casadio, S., Castelli, E., Papandrea, E., Dinelli, B. M., Pisacane, G., Burini, A., and Bojkov, B. R.: Total column water vapour from along track scanning radiometer series using thermal infrared dual view ocean cloud free measurements: The Advanced Infra-Red WAter Vapour Estimator (AIRWAVE) algorithm, Remote Sensing of Environment, 172, 1–14, https://doi.org/10.1016/j.rse.2015.10.037, 2016.

Chen, J. and Dai, A.: The atmosphere has become increasingly unstable during 1979–2020 over the Northern Hemisphere, Geophysical Research Letters, 50, e2023GL106 125, 2023.

Copernicus Climate Change Service and Climate Data Store: Aerosol properties gridded data from 1995 to present derived from satellite observation, DOI:10.24381/cds.239d815c, accessed: 2024-09-02, 2019.

Copernicus Climate Change Service and Climate Data Store: ERA5 hourly data on single levels from 1940 to present, DOI:10.24381/cds.adbb2d47, accessed: 2024-08-30, 2023.

Cox, C. and Munk, W.: Measurement of the Roughness of the Sea Surface from Photographs of the Sun's Glitter, Journal of the Optical Society of America, 44, 838, https://doi.org/10.1364/josa.44.000838, 1954.

Dauhut, T., Chaboureau, J. P., Haynes, P. H., and Lane, T. P.: The mechanisms leading to a stratospheric hydration by overshooting convection, Journal of the Atmospheric Sciences, 75, 4383–4398, https://doi.org/10.1175/JAS-D-18-0176.1, 2018.

Diedrich, H., Preusker, R., Lindstrot, R., and Fischer, J.: Retrieval of daytime total columnar water vapour from MODIS measurements over land surfaces, Atmospheric Measurement Techniques, 8, 823–836, https://doi.org/10.5194/amt-8-823-2015, 2015.

Diedrich, H., Wittchen, F., Preusker, R., and Fischer, J.: Representativeness of total column water vapour retrievals from instruments on polar orbiting satellites, Atmospheric Chemistry and Physics, 16, 8331–8339, https://doi.org/10.5194/acp-16-8331-2016, 2016.

Donlon, C., Berruti, B., Buongiorno, A., Ferreira, M.-H., Féménias, P., Frerick, J., Goryl, P., Klein, U., Laur, H., Mavrocordatos, C., et al.: The global monitoring for environment and security (GMES) sentinel-3 mission, Remote Sensing of Environment, 120, 37–57, 2012.

Doppler, L., Carbajal-Henken, C., Pelon, J., Ravetta, F., and Fischer, J.: Extension of radiative transfer code MOMO, matrix-operator model to the thermal infrared–Clear air validation by comparison to RTTOV and application to CALIPSO-IIR, Journal of Quantitative Spectroscopy and Radiative Transfer, 144, 49–67, 2014.

Dostalek, J. F., Grasso, L. D., Noh, Y.-J., Wu, T.-C., Zeitler , J. W., Weinman, H. G., Cohen, A. E. , and Lindsey, D. T.: Using GOES ABI Split-Window Radiances to Retrieve Daytime Low-Level Water Vapor for Convective Forecasting, E-Journal of Severe Storms Meteorology, 16, 1–19, https://doi.org/10.55599/ejssm.v16i2.79, 2021.

Doswell, C. A., Brooks, H. E., and Maddox, R. A.: Flash Flood Forecasting: An Ingredients-Based Methodology, Weather and Forecasting, 11, 560–581, https://doi.org/10.1175/1520-0434(1996)011<0560:FFFAIB>2.0.CO;2, 1996.

Durand, Y., Hallibert, P., Wilson, M., Lekouara, M., Grabarnik, S., Aminou, D., Blythe, P., Napierala, B., Canaud, J.-L., Pigouche, O., Ouaknine, J., and Verez, B.: The flexible combined imager onboard MTG: from design to calibration, Sensors, Systems, and Next-Generation Satellites XIX, 9639, 963 903, https://doi.org/10.1117/12.2196644, 2015.

El Kassar, J., Carbajal Henken, C., Preusker, R., and Fischer, J.: Optimal Estimation MSG-SEVIRI Clear-Sky Total Column Water Vapour Retrieval Using the Split Window Difference, Atmosphere, 12, 1256, https://doi.org/10.3390/atmos12101256, 2021.

EUMETSAT: EUMETSAT Data Store, https://data.eumetsat.int/.

EUMETSAT: MTGTD-505 FCI 1C Example Products for Compatibility Testing - Package Description, pp. 1–8, https://sftp.eumetsat.int/public/folder/UsCVknVOOkSyCdgpMimJNQ/User-Materials/Test-Data/MTG/MTG_FCI_L1C_RC72-20240113_TD-505_Feb2024/MTGTD-505FCI1CExampleProductsforCompatibilityTesting-PackageDescription.pdf, 2024a.

EUMETSAT: New MTG FCI test dataset (MTGTD-505), https://user.eumetsat.int/news-events/news/new-mtg-fci-test-dataset-mtgtd-505, 2024b.

Fabry, F.: The spatial variability of moisture in the boundary layer and its effect on convection initiation: Project-long characterization, Monthly Weather Review, 134, 79–91, 2006.

Fell, F. and Fischer, J.: Numerical simulation of the light field in the atmosphere–ocean system using the matrix-operator method, Journal of Quantitative Spectroscopy and Radiative Transfer, 69, 351–388, https://doi.org/10.1016/S0022-4073(00)00089-3, 2001.

Fischer, J.: High resolution spectroscopy for remote sensing of physical cloud properties and water vapour, 1988.

Gao, B.-C. and J., K. Y.: The MODIS Near-IR Water Vapor Algorithm Product ID : MOD05 - Total Precipitable Water, Algorithm Technical Background Document, pp. 1–25, %5CBiblioteca_Digital_SPR%5CGao1992_ATBD.pdf, 1992.

Gao, B. C., Montes, M. J., Davis, C. O., and Goetz, A. F.: Atmospheric correction algorithms for hyperspectral remote sensing data of land and ocean, Remote Sensing of Environment, 113, https://doi.org/10.1016/j.rse.2007.12.015, 2009.

García-Pereda, J., Rípodas, P., Lliso, L., Calbet, X., Martinez, M., Lahuerta, A., Bartolomé, V., , Gléau, H., Kerdraon, G., Péré, S., France, M., Moisselin, J.-M., Autones, F., Claudon, M., Jann, A., Wirth, A., Alonso, O., Fernandez, L., and Gallardo, J.: Use of NWCSAF NWC/GEO software package with MSG, Himawari-8/9 and GOES-13/16 satellites, in: EUMETSAT/AMS/NOAA, October, Boston, USA, 2019.

Hersbach, H., Bell, B., Berrisford, P., Hirahara, S., Horányi, A., Muñoz-Sabater, J., Nicolas, J., Peubey, C., Radu, R., Schepers, D., Simmons, A., Soci, C., Abdalla, S., Abellan, X., Balsamo, G., Bechtold, P., Biavati, G., Bidlot, J., Bonavita, M., Chiara, G. D., Dahlgren, P., Dee, D., Diamantakis, M., Dragani, R., Flemming, J., Forbes, R., Fuentes, M., Geer, A., Haimberger, L., Healy, S., Hogan, R. J.,

Hólm, E., Janisková, M., Keeley, S., Laloyaux, P., Lopez, P., Lupu, C., Radnoti, G., de Rosnay, P., Rozum, I., Vamborg, F., Villaume, S., and Thépaut, J. N.: The ERA5 global reanalysis, Quarterly Journal of the Royal Meteorological Society, 146, 1999–2049, https://doi.org/10.1002/qj.3803, 2020.

Hess, M., Koepke, P., and Schult, I.: Optical Properties of Aerosols and Clouds: The Software Package OPAC, Bulletin of the American Meteorological Society, 79, 831–844, https://doi.org/10.1175/1520-0477(1998)079<0831:OPOAAC>2.0.CO;2, 1998.

Hogan, R. J. and Matricardi, M.: Evaluating and improving the treatment of gases in radiation schemes: The Correlated K-Distribution Model Intercomparison Project (CKDMIP), Geoscientific Model Development, 13, 6501–6521, https://doi.org/10.5194/gmd-13-6501-2020, 2020.

Holben, B. N., Eck, T. F., Slutsker, I., Tanré, D., Buis, J. P., Setzer, A., Vermote, E., Reagan, J. A., Kaufman, Y. J., Nakajima, T., Lavenu, F., Jankowiak, I., and Smirnov, A.: AERONET—A federated instrument network and data archive for aerosol characterization, Remote Sensing of Environment, 66, 1–16, https://doi.org/https://doi.org/10.1016/S0034-4257(98)00031-5, 1998.

Hollstein, A. and Fischer, J.: Radiative transfer solutions for coupled atmosphere ocean systems using the matrix operator technique, Journal of Quantitative Spectroscopy and Radiative Transfer, 113, 536–548, https://doi.org/10.1016/j.jqsrt.2012.01.010, 2012.

Holmlund, K., Grandell, J., Schmetz, J., Stuhlmann, R., Bojkov, B., Munro, R., Lekouara, M., Coppens, D., Viticchie, B., August, T., et al.: Meteosat Third Generation (MTG): Continuation and innovation of observations from geostationary orbit, Bulletin of the American Meteorological Society, 102, E990–E1015, 2021.

Hu, J., Tang, S., Liu, H., and Min, M.: An operational precipitable water vapor retrieval algorithm for Fengyun-2F/VLSSR using a modified three-band physical split-window method, Journal of Meteorological Research, 33, 276–288, https://doi.org/10.1007/s13351-019-8111-4, 2019.

Hünerbein, A., Bley, S., Horn, S., Deneke, H., and Walther, A.: Cloud mask algorithm from the EarthCARE Multi-Spectral Imager: the M-CM products, Atmospheric Measurement Techniques, 16, 2821–2836, https://doi.org/10.5194/amt-16-2821-2023, 2023.

Iannone, R. Q., Niro, F., Goryl, P., Dransfeld, S., Hoersch, B., Stelzer, K., Kirches, G., Paperin, M., Brockmann, C., Gomez-Chova, L., Mateo-Garcia, G., Preusker, R., Fischer, J., Amato, U., Serio, C., Gangkofner, U., Berthelot, B., Iordache, M. D., Bertels, L., Wolters, E., Dierckx, W., Benhadj, I., and Swinnen, E.: Proba-V cloud detection Round Robin: Validation results and recommendations, 2017 9th International Workshop on the Analysis of Multitemporal Remote Sensing Images, MultiTemp 2017, https://doi.org/10.1109/Multi-Temp.2017.8035219, 2017.

Johns, R. H. and Doswell, C. A.: Severe Local Storms Forecasting, Weather and Forecasting, 7, 588–612, https://doi.org/10.1175/1520-0434(1992)007<0588:SLSF>2.0.CO;2, 1992.

Khordakova, D., Rolf, C., Grooß, J. U., Müller, R., Konopka, P., Wieser, A., Krämer, M., and Riese, M.: A case study on the impact of severe convective storms on the water vapor mixing ratio in the lower mid-latitude stratosphere observed in 2019 over Europe, Atmospheric Chemistry and Physics, 22, 1059–1079, https://doi.org/10.5194/acp-22-1059-2022, 2022.

Kleespies, T. J. and McMillin, L. M.: Retrieval of precipitable water from observations in the split window over varying surface temperatures, Journal of Applied Meteorology and Climatology, 29, 851–862, https://doi.org/https://doi.org/10.1175/1520-0450(1990)029<0851:ROPWFO>2.0.CO;2, 1990.

Knist, C., Kayser, M., Löffler, M., Vural, J., Schomburg, A., Görsdorf, U., Lauermann, F., Leinweber, R., Klink, S., and Lehmann, V.: DWD Pilotstation - Evaluating ground-based remote sensing systems for future observing networks, https://doi.org/10.5194/ems2022-119, 2022.

Koenig, M. and De Coning, E.: The MSG global instability indices product and its use as a nowcasting tool, Weather and Forecasting, 24, 272–285, https://doi.org/10.1175/2008WAF2222141.1, 2009.

Langley, S. P.: Annals of the Astrophysical Observatory of the Smithsonian Institution, Volume I., Monthly Weather Review, 30, 258–260, https://doi.org/10.1175/1520-0493-30.5.258, 1902.

Lindsey, D. T., Grasso, L., Dostalek, J. F., and Kerkmann, J.: Use of the GOES-R split-window difference to diagnose deepening low-level water vapor, Journal of Applied Meteorology and Climatology, 53, 2005–2016, https://doi.org/10.1175/JAMC-D-14-0010.1, 2014.

Lindsey, D. T., Bikos, D., and Grasso, L.: Using the GOES-16 split window difference to detect a boundary prior to cloud formation, Bulletin of the American Meteorological Society, 99, 1541–1544, https://doi.org/10.1175/BAMS-D-17-0141.1, 2018.

Lindsey, D. T., Heidinger, A. K., Sullivan, P. C., McCorkel, J., Schmit, T. J., Tomlinson, M., Vandermeulen, R., Frost, G. J., Kondragunta, S., and Rudlosky, S.: GeoXO NOAA's Future Geostationary Satellite System, Bulletin of the American Meteorological Society, 105, E660–E679, https://doi.org/10.1175/BAMS-D-23-0048.1, 2024.

Lindstrot, R., Preusker, R., Diedrich, H., Doppler, L., Bennartz, R., and Fischer, J.: 1D-Var retrieval of daytime total columnar water vapour from MERIS measurements, Atmospheric Measurement Techniques, 5, 631–646, https://doi.org/10.5194/amt-5-631-2012, 2012.

Lyapustin, A., Alexander, M. J., Ott, L., Molod, A., Holben, B., Susskind, J., and Wang, Y.: Observation of mountain lee waves with MODIS NIR column water vapor, Geophysical Research Letters, 41, 710–716, https://doi.org/10.1002/2013GL058770, 2014.

Martin, P. P., Durand, Y., Aminou, D., Gaudin-Delrieu, C., and Lamard, J.-L.: FCI instrument on-board MeteoSat Third Generation satellite: design and development status, in: International Conference on Space Optics—ICSO 2020, vol. 11852, pp. 125–140, SPIE, 2021.

Martinez, M. A., Calbet, X., and Ripodas, P.: Scientific and Validation Report for the iSHAI Processors of the NWC/GEO, https://www.nwcsaf.org/Downloads/GEO/2021/Documents/Scientific_Docs/NWC-CDOP3-GEO-AEMET-SCI-VR-iSHAI_v2.0.pdf, 2022.

Mather, J. H. and Voyles, J. W.: The arm climate research facility: A review of structure and capabilities, Bulletin of the American Meteorological Society, 94, 377–392, https://doi.org/10.1175/BAMS-D-11-00218.1, 2013.

Meerdink, S. K., Hook, S. J., Roberts, D. A., and Abbott, E. A.: The ECOSTRESS spectral library version 1.0, Remote Sensing of Environment, 230, 111 196, https://doi.org/10.1016/j.rse.2019.05.015, 2019.

Müller, J.: MSG Level 1.5 image data format description, EUM/MSG/ICD/105, p. 127, https://www-cdn.eumetsat.int/files/2020-05/pdf_ten_05105_msg_img_data.pdf, 2017.

Neelin, J. D., Martinez-Villalobos, C., Stechmann, S. N., Ahmed, F., Chen, G., Norris, J. M., Kuo, Y. H., and Lenderink, G.: Precipitation Extremes and Water Vapor: Relationships in Current Climate and Implications for Climate Change, Current Climate Change Reports, 8, 17–33, https://doi.org/10.1007/s40641-021-00177-z, 2022.

Pérez-Ramírez, D., Whiteman, D. N., Smirnov, A., Lyamani, H., Holben, B. N., Pinker, R., Andrade, M., and Alados-Arboledas, L.: Evaluation of AERONET precipitable water vapor versus microwave radiometry, GPS, and radiosondes at ARM sites, Journal of Geophysical Research, 119, 9596–9613, https://doi.org/10.1002/2014JD021730, 2014.

Peters, J. M., Nielsen, E. R., Parker, M. D., Hitchcock, S. M., and Schumacher, R. S.: The impact of low-level moisture errors on model forecasts of an MCS observed during PECAN, Monthly Weather Review, 145, 3599–3624, 2017.

Phillips, P., Bonsignori, R., Schluessel, P., Schmülling, F., Spezzi, L., Watts, P., and Zerfowski, I.: Overview of calibration and validation activities for the EUMETSAT polar system: second generation (EPS-SG) visible/infrared imager (METimage), Proc SPIE, 10000, 100 000S–1, https://doi.org/10.1117/12.2240938, 2016.

Pinty, B. and Verstraete, M. M.: GEMI: a non-linear index to monitor global vegetation from satellites, Vegetatio, 101, 15–20, https://doi.org/10.1007/BF00031911, 1992.

Preusker, R., Henken, C. C., and Fischer, J.: Retrieval of daytime total column water vapour from OLCI measurements over land surfaces, Remote Sensing, 13, 1–23, https://doi.org/10.3390/rs13050932, 2021.

Púčik, T., Groenemeijer, P., Rỳva, D., and Kolář, M.: Proximity soundings of severe and nonsevere thunderstorms in central Europe, Monthly Weather Review, 143, 4805–4821, https://doi.org/10.1175/MWR-D-15-0104.1, 2015.

Rodgers, C. D.: Inverse methods for atmospheric sounding - theory and practice, 2, 238, https://doi.org/10.1142/9789812813718, 2000.

Rothman, L., Rinsland, C., Goldman, A., Massie, S., Edwards, D., Flaud, J.-M., Perrin, A., Camy-Peyret, C., Dana, V., Mandin, J.-Y., Schroeder, J., McCann, A., Gamache, R., Wattson, R., Yoshino, K., Chance, K., Jucks, K., Brown, L., Nemtchinov, V., and Varanasi, P.: The HITRAN Molecular Spectroscopic Database and HAWKS (HITRAN Atmospheric Workstation): 1996 Edition, Journal of Quantitative Spectroscopy and Radiative Transfer, 60, 665–710, https://doi.org/10.1016/S0022-4073(98)00078-8, 1998.

Schmetz, J., Pili, P., Tjemkes, S., Just, D., Kerkmann, J., Rota, S., and Ratier, A.: An Introduction to Meteosat Second Generation (MSG), Bulletin of the American Meteorological Society, 83, 991–991, https://doi.org/10.1175/bams-83-7-schmetz-1, 2002.

Schmidt, G. A., Ruedy, R. A., Miller, R. L., and Lacis, A. A.: Attribution of the present-day total greenhouse effect, Journal of Geophysical Research Atmospheres, 115, 1–6, https://doi.org/10.1029/2010JD014287, 2010.

Setvák, M., Lindsey, D. T., Rabin, R. M., Wang, P. K., and Demeterová, A.: Indication of water vapor transport into the lower stratosphere above midlatitude convective storms: Meteosat Second Generation satellite observations and radiative transfer model simulations, Atmospheric Research, 89, 170–180, https://doi.org/10.1016/j.atmosres.2007.11.031, 2008.

Sisterson, D. L., Peppler, R. A., Cress, T. S., Lamb, P. J., and Turner, D. D.: The ARM Southern Great Plains (SGP) Site, Meteorological Monographs, 57, 6.1–6.14, https://doi.org/10.1175/amsmonographs-d-16-0004.1, 2016.

Skakun, S., Wevers, J., Brockmann, C., Doxani, G., Aleksandrov, M., Batič, M., Frantz, D., Gascon, F., Gómez-Chova, L., Hagolle, O., López-Puigdollers, D., Louis, J., Lubej, M., Mateo-García, G., Osman, J., Peressutti, D., Pflug, B., Puc, J., Richter, R., Roger, J. C., Scaramuzza, P., Vermote, E., Vesel, N., Zupanc, A., and Žust, L.: Cloud Mask Intercomparison eXercise (CMIX): An evaluation of cloud masking algorithms for Landsat 8 and Sentinel-2, Remote Sensing of Environment, 274, https://doi.org/10.1016/j.rse.2022.112990, 2022.

Thomas, G. E., Carboni, E., Sayer, A. M., Poulsen, C. A., Siddans, R., and Grainger, R. G.: Satellite Aerosol Remote Sensing over Land, January, https://doi.org/10.1007/978-3-540-69397-0, 2009.

Trenberth, K. E., Dai, A., Rasmussen, R. M., and Parsons, D. B.: The Changing Character of Precipitation, Bulletin of the American Meteorological Society, 84, 1205–1218, https://doi.org/10.1175/BAMS-84-9-1205, 2003.

Turner, D. D., Clough, S. A., Liljegren, J. C., Clothiaux, E. E., Cady-Pereira, K. E., and Gaustad, K. L.: Retrieving liquid water path and precipitable water vapor from the atmospheric radiation measurement (ARM) microwave radiometers, IEEE Transactions on Geoscience and Remote Sensing, 45, 3680–3689, https://doi.org/10.1109/TGRS.2007.903703, 2007.

Valdés, E. A. M., Morris, B. M., and Demory, B. O.: Monitoring precipitable water vapour in near real-time to correct near-infrared observations using satellite remote sensing, Astronomy and Astrophysics, 649, https://doi.org/10.1051/0004-6361/202039629, 2021.

Van Baelen, J., Reverdy, M., Tridon, F., Labbouz, L., Dick, G., Bender, M., and Hagen, M.: On the relationship between water vapour field evolution and the life cycle of precipitation systems, Quarterly Journal of the Royal Meteorological Society, 137, 204–223, https://doi.org/10.1002/qj.785, 2011.

Van Ulden, A. P. and Wieringa, J.: Atmospheric boundary layer research at Cabauw, Boundary-Layer Meteorology, 78, 39–69, https://doi.org/10.1007/BF00122486, 1996.

Vidot, J. and Borbás, É.: Land surface VIS/NIR BRDF atlas for RTTOV-11: Model and validation against SEVIRI land SAF albedo product, Quarterly Journal of the Royal Meteorological Society, 140, 2186–2196, https://doi.org/10.1002/qj.2288, 2014.

Ware, R. H., Fulker, D. W., Stein, S. A., Anderson, D. N., Avery, S. K., Clark, R. D., Droegemeier, K. K., Kuettner, J. P., Minster, J. B., and Sorooshian, S.: Suominet: A real-time national GPS network for atmospheric research and education, Bulletin of the American Meteorological Society, 81, 677–694, https://doi.org/10.1175/1520-0477(2000)081<0677:SARNGN>2.3.CO;2, 2000.

Wevers, J., Müller, D., Scholze, J., Kirches, G., Quast, R., and Brockmann, C.: Sentinel-2 MSI IdePix ATBD, https://zenodo.org/record/5788067, 2021.

Wiegner, M. and Gasteiger, J.: Correction of water vapor absorption for aerosol remote sensing with ceilometers, Atmospheric Measurement Techniques, 8, 3971–3984, https://doi.org/10.5194/amt-8-3971-2015, 2015.